PRESSURE TRANSIENT ANALYSIS OF FRACTURED WELLS IN SHALE RESERVOIRS

by

Cong Wang

A thesis submitted to the Faculty and the Board of Trustees of the Colorado School of Mines in partial fulfillment of the requirements for the Master degree (Petroleum Engineering).

Golden, Colorado

Date _____

Signed: _____

Cong Wang

Signed: _____

Dr. Yu-Shu Wu

Advisor

Golden, Colorado

Date _____

Signed: _____

Dr. William Fleckenstein

Professor and Head

Department of Petroleum

ABSTRACT

In this study, an unconventional reservoir simulator is developed, which is based on a general black-oil simulator "MSFLOW". We incorporate several non-linear flow mechanisms (Klinkenberg effects, non-Darcy flow, gas adsorption and geomechanics effect) into the simulator. We also present a hybrid-fracture conceptual model to describe different types and scales of fractures from explicit hydraulic fractures and fracture network in simulated reservoir volume (SRV) to distributed natural fractures, microfractures, and tight sand matrix. Numerical formulation and its implementation of the simulator are validated using analytical results. Then this simulator is used to study gas flow in shale reservoirs.

Three application examples are presented with this unconventional reservoir gas simulator. 1) We evaluate each of the above-mentioned non-linear flow mechanisms in a horizontal well, multi-stage hydraulic fractures reservoir scenario to see their influence on production. 2) We conduct a study of the "hydraulic fracture-matrix" linear flow and propose a methodology to estimate the total hydraulic fracture and matrix contact area. 3) We complete a history match of field data. These examples demonstrate the applicability of the reservoir simulator to modeling unconventional gas reservoirs.

TABLE OF CONTENTS

LIST OF FIGURES

LIST OF TABLES

ACKNOWLEDGEMENTS

First I would like to thank my advisor Dr. Yu-Shu Wu for his support, encouragement and guidance during this work. I would also like to thank my committee, Dr. Xiaolong Yin, Dr. Azra Tutuncu and Dr. Erdal Ozkan for reading the thesis and providing valuable comments. I would like to express my appreciation to Dr. Ozkan for sharing his prescriptive relevant studies and field data for the case study. I also wish to thank the rest of the faculty in Petroleum Engineering Department for their supports and contributions to my academic achievements.

Special thanks are due to my parents for supporting and encouraging my education from the very beginning. I am also very thankful to my Chinese friends at Mines, who have shared with me the experience of going abroad for advanced education.

Finally, I like to thank the organizations and companies supporting Energy Modeling Group (EMG) and Unconventional Natural Gas and Oil Institute (UNGI).

CHAPTER 1

INTRODUCTION

Unconventional gas resources from tight sand and shale reservoirs have received a great attention in the past decade around the world, because of their large reserves as well as technical advances in developing these resources. As a result of the improved horizontal drilling and hydraulic fracturing technologies, significant progresses are being made towards commercial gas production from such reservoirs, as demonstrated in the US. However, understandings and technologies needed for effective development of unconventional reservoirs are still far behind the industry needs, e.g., gas recovery rates from those unconventional resources remain very low.

There are efforts in the literature on how to model gas flow in shale gas reservoirs using various approaches from modified commercial simulators to analytical solutions, leading to limited success. Compared with conventional reservoirs, gas flow in ultra-low permeability unconventional reservoirs is subject to more nonlinear, coupled processes, including nonlinear adsorption/desorption, non-Darcy flow (at high flow rate and low flow rate), and strong rock-fluid interaction, and rock deformation within nano-pores or micro-fractures, coexisting with complex flow geometry and multi-scaled heterogeneity. Therefore, quantifying flow in unconventional gas reservoirs has been a significant challenge and traditional REV-based Darcy law, for example, may not be generally applicable.

1.1 Introduction of MSFLOW

In this research, the numerical coding work is based on a general black-oil simulator, MSFLOW, developed by Dr. Yu-Shu Wu to model three-phase flow of Newtonian and non-Newtonian fluids of oil, gas, and water in multidimensional porous and fractured reservoirs (Wu, 1998). The MSFLOW code is designed to simulate multiphase flow processes involved in oil and/or gas production and is particularly applicable for feasibility and prediction studies to evaluate different operations and schedules that may be taken for enhanced oil/gas recovery from an oil reservoir undergoing waterflooding for a long time.

The MSFLOW simulator takes into account simultaneous flow of the three phases of oil, gas and water through porous and fractured geological media. Fluid flow in the three phases occurs under pressure, viscous, and gravity forces according to the Darcy's law. The interference between the phases during flowing through porous media is described by means of relative permeability and capillary pressure functions. The governing partial differential equations for mass balance equations of the three fluid phases are handled using the integral finite difference (IFD) numerical method for the spatial discretization. The time is discretized using a first order finite difference. The final discrete non-linear equations are solved using a Newton iteration scheme fully implicitly in general or with an Adaptive Implicit Method (AIM) approach as an option. The IFD approach has proven to be computationally efficient in modeling highly non-linear three-phase flow problems and at the same time it has flexibility in handling complicated geometry or irregularity of a reservoir domain.

1.2 Outline of the Thesis

This thesis explores a numerical approach to describe the gas flow behavior in unconventional reservoirs, e.g., shale gas and tight gas reservoirs. The scope includes the incorporation of some important flow mechanisms into MSFLOW, which are rarely considered for conventional reservoirs but essential for unconventional reservoirs. The ultimate goal of this work is to help in understanding flow mechanisms for shale gas or tight gas production, to determine the influences on pressure and production behavior by considering these mechanisms, and to provide a two-phase (water and gas) unconventional simulator for applications and modeling studies in the field.

The objective of Chapter 2 is to describe flow mechanisms for unconventional reservoirs currently accepted by the academy and industry and to state the problems that this thesis will address. Both the non-linear flow mechanisms, such as Klinkenberg effect, non-Darcy flow, gas adsorption/desorption, and geomechanics effect as well as fracture models like natural fractures and hydraulic fractures are discussed.

Chapter 3 presents the numerical approach to build this model on from the mass conservation equation, time and space discretization of these equations, incorporation of the above mentioned non-linear mechanisms and numerical schemes for horizontal wells, natural fractures and hydraulic fractures. Chapter 4 focuses mainly on validation of the numerical formulation and its implementation. In addition, analytical solutions are derived for 1D linear or radial problem considering Klinkenberg effect, non-Darcy flow, gas adsorption, and geomechanics and used to verify the numerical model. This guarantees the accuracy of numerical work and helps in further applications.

Simulation results and model applications are described in Chapter 5, in which three examples are studied. The first one presents introduction about how to build a hybrid-fracture grid system. "Fracture-matrix linear flow" is studied in this case. The second example is application of a field example. It gives an evaluation on whether we need to consider the non-linear flow mechanisms, such as Klinkenberg effect, gas adsorption, and geomechanics effect based on some limited data. The third one studies a field example. With the well-built unconventional flow model, history match work is done on comparison of daily production rate and pressure profiles. Finally the conclusions from this work and future plans are presented in Chapter 6.

CHAPTER 2

STATEMENT OF THE PROBLEM

There are two main facts making unconventional reservoirs different from conventional reservoirs. One is the extremely low formation permeability. Permeability in shale gas or tight gas formation is about or lower than 0.001md, while that in conventional formation it usually ranges from 10md to 1,000md. Because of the extremely low permeability, many nonlinear flow mechanisms, such as Klinkenberg effect (slippage gas flow), non-Darcy flow, gas adsorption/desorption and geomechanics effect, may not be ignored in flow calculation and reservoir characterization. The other difference is relying on long horizontal wells. Traditional vertical wells are not enough for economical production in unconventional reservoirs and horizontal wells with multi-stage hydraulic fractures are preferred by industry. Traditional reservoir simulators are generally inappropriate to model fluid flow in unconventional reservoirs, as they are not designed to handle these two differences. If reservoir engineers insist on unconventional reservoir simulation using a traditional simulator, systematical errors will be introduced.

Flow behavior in shale gas and tight gas reservoirs is characterized by single-phase (gas) and/or multi-phase (gas, gas condensate and/or brine) flow and transport in extremely low-permeability, highly heterogeneous porous/fractured, and stress-sensitive rock. Compared with the flow in conventional reservoirs, gas flow in ultra-low permeability unconventional reservoirs is subject to more nonlinear, coupled processes, including nonlinear adsorption/desorption, non-Darcy flow (at both high flow rate and

low flow rate), strong rock-fluid interaction, and rock deformation within nanopores or micro-fractures, coexisting with complex flow geometry and multi-scaled heterogeneity. Therefore, quantifying flow in unconventional gas reservoirs has been a significant challenge and traditional REV-based Darcy law approaches, for example, may not be in general applicable. Because of the low permeability and highly nonlinear or non-Darcy flow behavior in such shale or tight rock, the traditional, Darcy's law based simulators will be unable to handle nonlinearity of the flow in shale gas reservoirs. Currently, there is little in basic understanding on how these complicated flow behavior impacts on gas flow and ultimate gas recovery in such reservoirs. In particular, there are few effective reservoir simulators currently available or few modeling studies (e.g., Kelkar and Atiq, 2010) in the industry for assisting reservoir engineers to model and develop the unconventional natural gas resources.

In this chapter, we first discuss non-linear mechanisms that are essential in characterizing unconventional reservoirs gas flow, from their physical backgrounds, their theoretical analysis to mathematical models. Then we introduce modeling approaches for handling fractures in unconventional reservoir simulation.

2.1 Non-Linear Flow Mechanisms

In this part, several non-linear flow mechanisms such as Klinkenberg effect, gas adsorption, non-Darcy flow and geomechanics will be introduced in both physical and numerical approaches.

2.1.1 Klinkenberg Effect

The Klinkenberg effect (Klinkenberg, 1941) was observed that the gas apparent permeability depends on the reciprocal of the flowing pressure. This phenomenon is also known as slip velocity (molecular streaming or Knudsen flow). From the Kundt and

Warburg's molecular theory (Knudt and Warburg, 1875), the following expression for apparent permeability was derived by Klinkenberg:

$$k_g = k_\infty \left(1 + \frac{b}{P_g}\right) \tag{2.1}$$

where k_∞ is constant, absolute gas-phase permeability under very large gas-phase pressure (where the Klinkenberg effect is minimized); and b is the Klinkenberg b-factor and could be pressure or temperature dependent, accounting for gas-slippage effect.

Klinkenberg effect has been practically ignored in conventional gas reservoir studies, except in some cases when analyzing pressure responses or flow near gas production wells at very low pressure. This is because of larger pore size and relatively high pressure existing in those conventional gas reservoirs. In shale gas reservoirs, however, the formation is characterized by extremely low permeability from subnanodarcys to microdarcys and is different for different type of shale, even under the similar porosity, stress, or pore pressure. As summarized by Wang et al. (2009), the permeability of deep organic-lean mud rocks ranges from smaller than to tens of nanodarcys, while permeability values in organic-rich gas shale from subnanodarcys to tens of microdarcys. Thus the Klinkenberg or slippage effect is expected to be significant, because of the nano-size pores of such rock, even under high pressure condition. Wang et al. (2009) show that gas permeability in the Marcellus Shale increases from 19.6 μD at 1,000 psi to 54 μD at 80 psi, because of the strong slippage effect.

Apart from the above formulation, dynamic gas slippage theory was proposed based on the assumption that gas travels under the influence of a concentration field

(random molecular flow) and a pressure field (macroscopic flow) (Ertekin et al. 1986). According to this theory, Klinkenberg factor is not a constant anymore but a pressure dependent value. They gave the expression of Klinkenberg factor as below:

$$b = \frac{Pc_g D\mu}{k_g} \tag{2.2}$$

where P is pressure; c_g is gas compressibility; D is diffusivity coefficient; μ is gas viscosity and k_g is permeability constant. Figure 2.1 shows the Klinkenberg effect, i.e., effect of pore pressure on gas permeability, using experimental data from the Marcellus Shale, with a confining pressure of 3,000 psi.

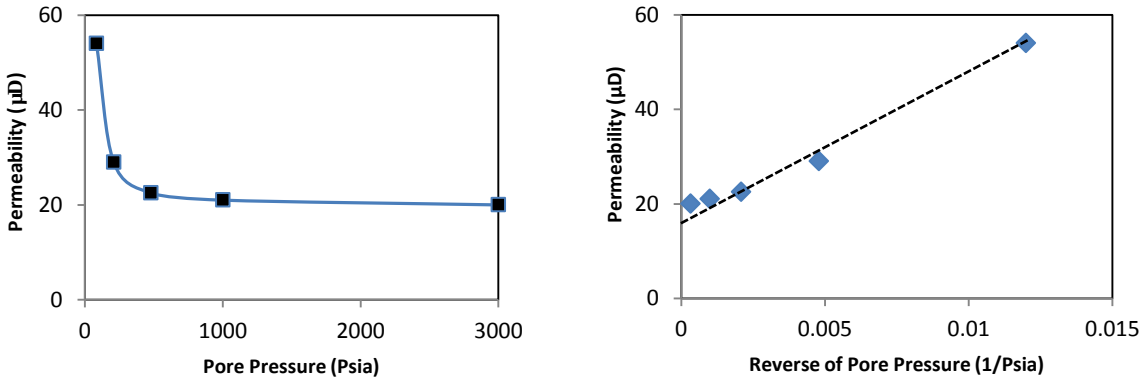

Figure 2.1 Effect of pore pressure on gas permeability in the Marcellus Shale, with a confining pressure of 3,000 psi (Soeder, 1988; Wang et al. 2009)

2.1.2 Gas Adsorption/Desorption

Natural gas in shale formations is present both as a free gas phase in pores and as an adsorbed gas phase on solids. In shale gas reservoirs, gas or methane molecules are adsorbed to the carbon-rich components, i.e. kerogen (Mengal and Wattenbarger, 2011;

EIA, 2011; Wu et al. 2012). The adsorbed gas represents significant quantities of total gas reserves (20-80%) as well as recovery rates, which cannot be ignored in any model or modeling analysis. Past studies have found that methane molecules are adsorbed mainly to the carbon-rich components, i.e. kerogen, correlated with total organic content (TOC). As the pressure decreases with continuous gas production from reservoirs, more adsorbed gas is released from solid to free gas phase, contributing to the flow or production.

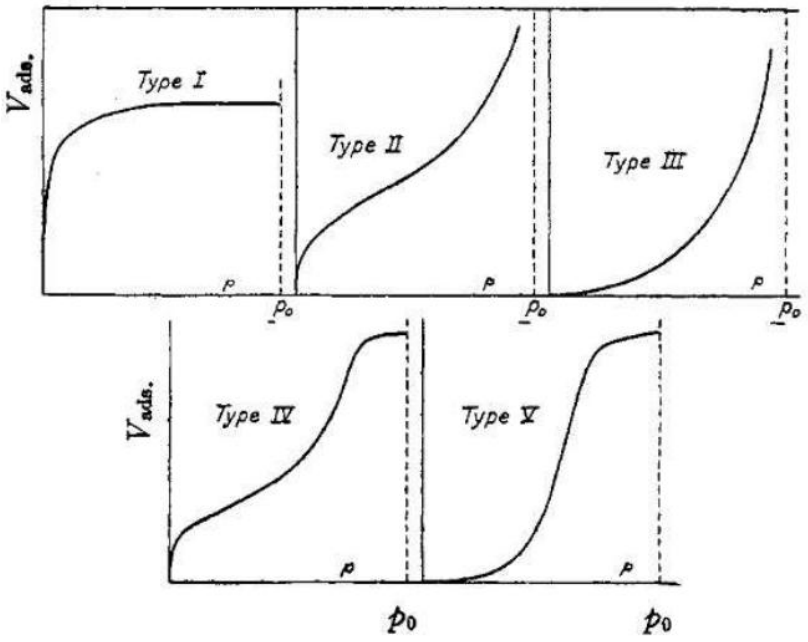

Figure 2.2 Five types of adsorption isotherms (Brunauer et al. 1940)

The BDDT theory (Brunauer et al. 1940) classifies the adsorption isotherms into five types as shown in Figure 2.2. Type I is the classical Langmuir isotherm. Their shapes reflect the complexity and the size of the kerogen pore geometry. Due to the high heterogeneity and multiple adsorption layers, the actual adsorption shape may be different from the classic Langmuir isotherm. However, Langmuir isotherm is widely

accepted by academy and industry (e.g., Silin and Kneafsey, 2011) and it will be adopted in this research.

In this research, the mass of adsorbed gas in formation volume is correlated to gas pressure according to the Langmuir's isotherm (1918). To calculate the amount of adsorbed gas, gas content and sorption isotherm need to be determined in laboratory using core samples. Gas content is the amount of total gas adsorbed on the surface of reservoir rock, whereas sorption isotherm is the capacity of the reservoir rock to hold adsorbed gas with respect to pressure at constant temperature. Then, it is used to define the relationship of pressure and gas storage capacity of the reservoir rock.

The Langmuir's isotherm is in general used to describe the gas content, V_E, typically measured as cubic feet of gas per ton of net shale (Mengal and Wattenbarger, 2011; EIA, 2011),

$$V_E = V_L \frac{P}{P + P_L} \tag{2.3}$$

where V_E is the gas content or Langmuir's volume in scf/ton (or standard volume adsorbed per unit rock mass); P is reservoir gas pressure; and P_L is Langmuir's pressure, the pressure at which 50% of the gas is desorbed. In general, Langmuir's volume, V_L, is a function of the organic richness (or TOC) and thermal maturity of the shale and one example for gas adsorbed curve is illustrated in Figure 2.3 for the Marcellus Shale (EIA, 2011).

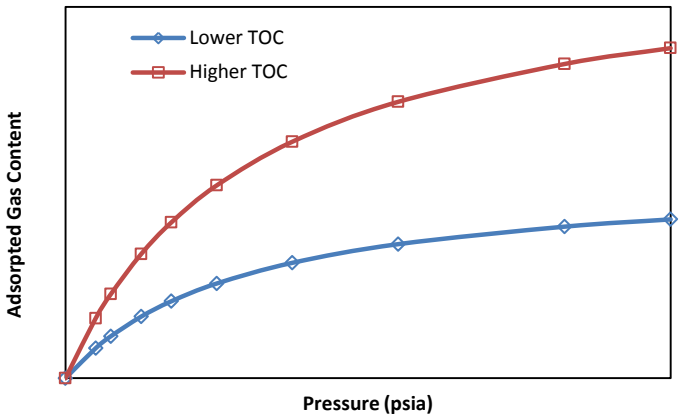

Figure 2.3 Marcellus Shale Adsorbed Gas Content (EIA, 2011)

2.1.3 Non-Darcy Flow

Unconventional reservoir dynamics is characterized by highly nonlinear behavior of multiphase flow in extremely low-permeability rock, coupled by many co-existing physical processes, e.g., non-Darcy flow. Blasingame (2008) and Moridis et al. (2010) provide comprehensive review of flow mechanisms in unconventional shale gas reservoirs. Both studies point out that non-laminar/non-Darcy flow concept of high-velocity may turn out to be important in shale gas production. The non-laminar/non-Darcy flow concept of high-velocity flow of gas flow in shale gas reservoirs may not be represented by Darcy's law and the *Forchheimer* equation is probably sufficient for many applications.

Forchheimer investigated fluid flow through porous media in the high velocity regime. As flow velocity increases, the inertial effects dominating the flow were observed. To quantify these high velocity inertial effects, he suggested the inclusion of an inertial

term to represent the kinetic energy of the fluid to the Darcy equation, given as the follows:

$$-\left(\nabla\Phi_\beta\right)=\frac{\mu_\beta}{k_{r\beta}}\,k\,\mathbf{v}_\beta+\beta_\beta\rho_\beta\mathbf{v}_\beta\left|\mathbf{v}_\beta\right| \tag{2.4}$$

where β_β is the effective non-Darcy flow coefficient with a unit m^{-1} for fluid β under multiphase flow conditions; $\mathbf{v}_\beta$ is the Forchheimer velocity vector. It is cumbersome to evaluate the Forchheimer coefficient β_β in theoretical approach or for practical applications. This coefficient is usually obtained from experiment data. The non-Darcy flow correlation from Tek et al. (1962) may be used to evaluate the non-Darcy flow coefficient β_β versus porosity and permeability as follows:

$$\beta_\beta=\frac{C_\beta}{k^{5/4}\phi^{3/4}} \tag{2.5}$$

Apart from Tek's work, Ergun (1952) worked for fluid flow through packed columns. Based on the work, Ergun proposed another expression for the Forchheimer coefficient β_β:

$$\beta_\beta=\frac{C_E}{\sqrt{K}} \tag{2.6}$$

where C_E is called Ergun constant and used to quantify inertial effects. K is the porous media permeability.

2.1.4 Geomechanics Effect

Geomechanics plays a critical role in successfully optimizing unconventional reservoir exploitation. The scope spans from the well stability, hydraulic fracturing process design to reservoir management. In conventional oil and gas reservoirs, effect of geomechanics on rock deformation and permeability is generally small and has been mostly ignored in practice. However, in unconventional shale formations with nano-size pores or nano-size microfractures, such geomechanics effect can be relatively large and may have a significant impact on both fracture and matrix permeability, which has to be considered in general. Wang et al. (2009) shows that permeability in the Marcellus Shale is pressure-dependent and decreases with an increase in confining of pore pressure (or effective stress). The effect of confining pressure on permeability is caused by a reduction of porosity. Bustin et al. (2008) report the effect of stress (confining pressure) in Barnett, Muskwa, Ohio, and Woodford shales and show that degree of permeability reduction with confining pressure is significantly higher in shales than that in consolidated sandstone or carbonate.

The effective porosity, permeability, and capillary pressure of rock are assumed to correlate with the mean effective stress (σ'_m), defined as,

$$\sigma'_m = \sigma_m(x, y, z, P) - \alpha P \tag{2.7}$$

where α is the Biot constant

$$\sigma_m(x, y, z, P) = (\sigma_x(x, y, z, P) + \sigma_y(x, y, z, P) + \sigma_z(x, y, z, P))/3 \tag{2.8}$$

where σ_x, σ_y, and σ_z are total stress in x, y, and z- directions, respectively. With the definition of the mean effective stress in Equation (2.8), the effective porosity of

formation (fractures or porous media) is defined as a function of mean effective stress only,

$$\phi = \phi\left(\sigma'_m\right) \tag{2.9}$$

Similarly, the intrinsic permeability is related to the effective stress, i.e.,

$$k = k\left(\sigma'_m\right) \tag{2.10}$$

Several correlations have been used for porosity as a function of effective stress and permeability as a function of porosity (Winterfeld and Wu, 2012 and 2012a). A theory of hydrostatic poroelasticity (Zimmerman et al. 1986) has been proposed that accounts for the coupling of rock deformation with fluid flow inside the porous rock. Porosity as a function of effective stress is derived from this theory,

$$d\phi = -\left[\frac{1}{K}(1-\phi) - C_r\right] d\sigma'_m \tag{2.11}$$

where K is bulk modulus; and C_r is rock grain compressibility.

Porosity is the ratio of fluid to bulk (solid plus fluid) volume. Bulk volume, V, is related to volumetric strain, ε_v, by

$$V = V_0(1-\varepsilon_v) = V_i \frac{(1-\varepsilon_v)}{(1-\varepsilon_{v,i})} \tag{2.12}$$

where V_0 is zero strain volume and subscript i refers to reference conditions. .

It has to be mentioned that Figure 2.4 from Wang et al. (2009) presents the permeability measurement from core plugs where potential natural microfractures in core

plugs play an important role for the connectivity. If crushed samples are used to measure the matrix permeability only by eliminating natural and drilling induced microfactures, the permeability value is one or two orders lower. The geomechanics has a much stronger impact on the fracture than on the matrix. So, when using a dual-porosity approach in the modeling, if microfractures are considered as a part of the matrix media, the above relations can be directly applied. However, if microfractures are considered as a part of the fractured media, the geomechanics effect is more complex because fracture conductivities are subjected to different laws depending on microfractures, partially propped fractures or propped fractures (Cipolla et al. 2009).

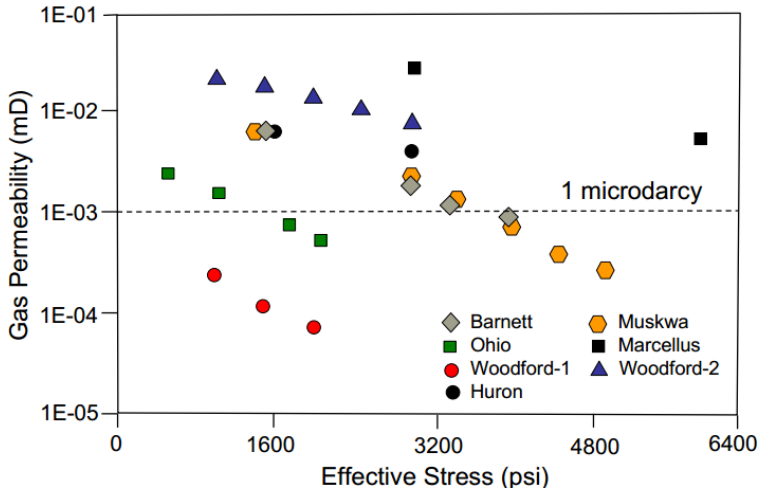

Figure 2.4 Effect of confining pressure on gas permeability in gas. (Wang et al. 2009)

2.2 Fracture Conceptual Models

Handling flow through fractured media is critical in shale gas reservoir simulation, because gas production from such low-permeability formations relies on fractures, from hydraulic fractures/network to various-scaled natural fractures, to provide flow channels

for gas flow into producing wells. Therefore, any unconventional reservoir simulator must have the capability of handling fractured media. The published modeling exercises in the literature have paid a lot of attention to model fractures in shale gas formations (e.g., Cipolla, 2009; Freeman et al. 2009a; 2009b; 2010; Moridis et al. 2010; Cipolla et al. 2010; Rubin, 2010; Wu et al. 2012). However, it should be pointed out that there have been very few studies carried out to address the critical issues how to accurately simulate fractured unconventional gas reservoirs or to select the best approach for modeling a given shale gas formation. Most of the modeling exercises use commercial reservoir simulators, developed for conventional fractured reservoir simulation, which have very limited capabilities of modeling multi-scaled or complicated fractured reservoirs. On the other hand, in order to simulate fractured unconventional gas reservoirs, more efforts on model developments are needed from new conceptual models to in-depth modeling studies of laboratory to field scale application.

2.2.1 Double Porosity Model

Double-porosity model is an idealized model proposed by Warren and Root in 1963, as shown in Figure 2.5. In the double-porosity model, a flow domain is composed of matrix blocks with low permeability, embedded in a network of interconnected fractures. Global flow and transport in the formation occur only through the fracture system, conceptualized as an effective continuum. This model treats matrix blocks as spatially distributed sinks or sources to the fracture system without accounting for global matrix-matrix flow.

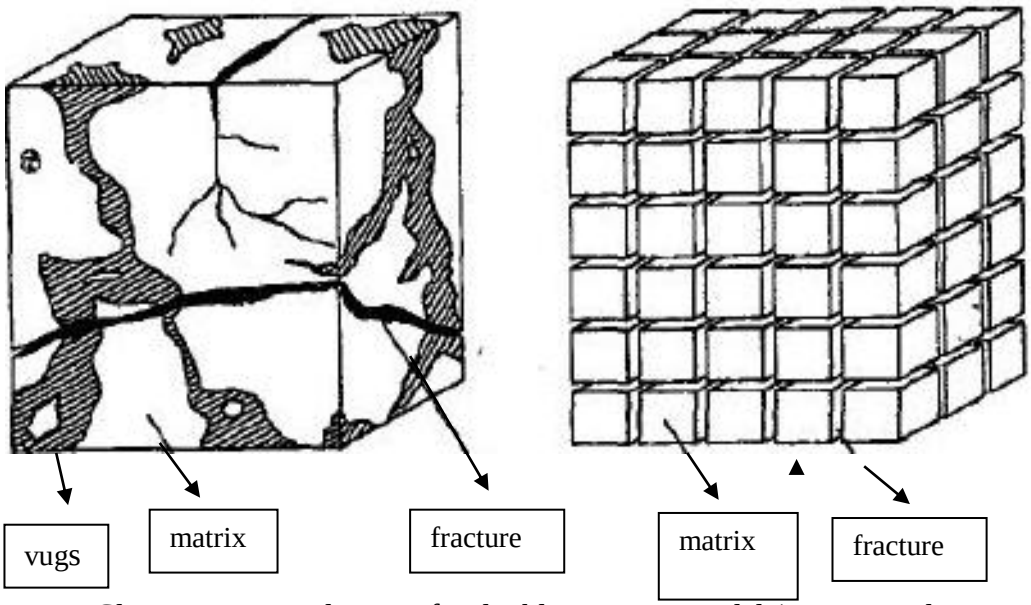

Figure 2.5 Classic conceptualization for double-porosity model (Warren and Root, 1963)

2.2.2 Multiple-Interacting Continua (MINC)

Pruess and Narasimhan (1985) introduced the concept of Multiple-Interacting Continua (MINC) to model heat and multiphase fluid flow in multidimensional, fractured porous media. The MINC concept is able to describe gradients of pressures, temperatures, or concentrations near matrix surface and inside the matrix—by further subdividing individual matrix blocks with one- or multidimensional strings of nested meshes, as shown in Figure 2.6. Therefore, the MINC method treats interporosity flow in a fully transient manner by computing the gradients which drive interporosity flow at the matrix-fracture interface. As a result, the MINC model in general provides a better numerical approximation for transient fracture-matrix interactions than the double-porosity model when the pressure, temperature or concentration distribution in matrix is hard to reach the pseudo-steady state. For shale gas reservoirs, the average fracture spacing could be large and the matrix permeability is extremely low. Therefore, matrix pressure distribution is in

transient state most of the time. Compared with the double-porosity model, MINC is more suitable for handling this fractured reservoir. However, the adoption of MINC will be more computational intensive because we need to subdivide the original matrix grid into at least 10 strings of nested meshes and the double-porosity model need only two. What's more, the MINC approach may not be applicable to systems in which fracturing is so sparse that the fractures cannot be approximated as a continuum (Moridis et al. 2010).

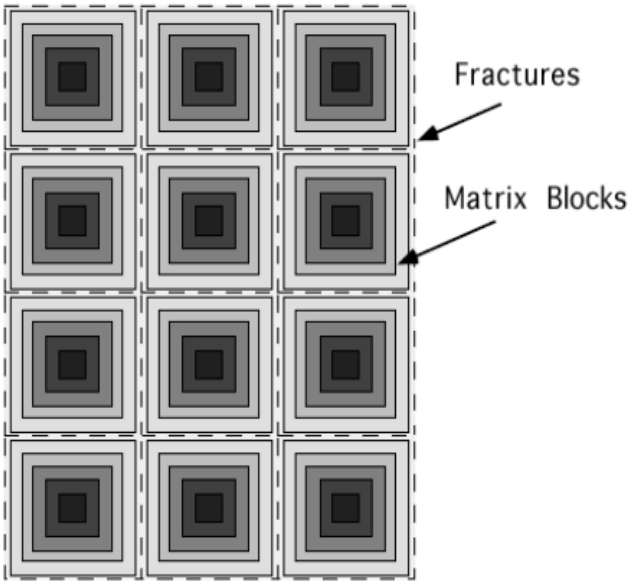

Figure 2.6 Schematic of MINC (multiple interacting continua) Concept (Pruess and Narasimham, 1985)

2.2.3 Explicit Discrete Fracture Modeling Approach

Explicit discrete-fracture modeling approach (i.e., simulating each of fractures explicitly in the reservoir model) is, in principle, a more rigorous model, as shown in Figure 2.7. Compared with dual-porosity models, this approach can be applied to

disconnected fractured media. In addition, it is suited for the modeling of a small number of large-scale fractures, which may dominate the flow (Karimi-Fard et al. 2004). In the past, the application of this method to field simulation studies of conventional reservoirs has been limited, because of the computational intensity involved, as well as the lack of detailed knowledge of fracture and matrix geometric properties and their spatial distributions at a given subsurface site. However, this approach is very suitable for handling hydraulic fractures, because there are few hydraulic fractures as well as better estimates of their spatial distributions when compared to natural fractures.

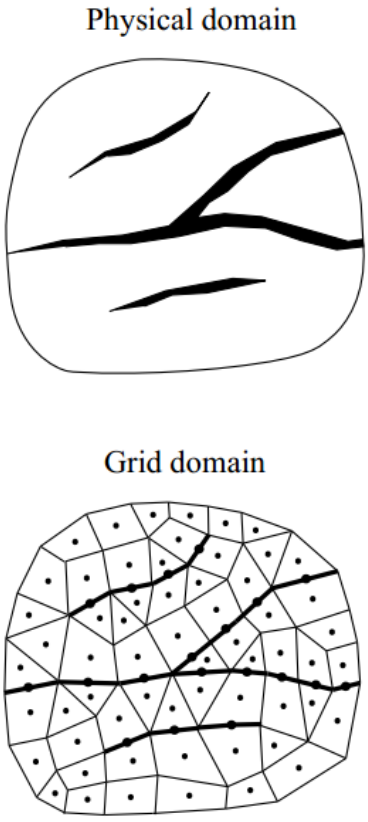

Figure 2.7 A two-dimensional example of discrete fracture model (Karimi-Fard et al. 2004)

CHAPTER 3

MATHEMATICAL AND NUMERICAL MODELS

The MSFLOW codes were developed for the black-oil model study. This research project started from MSFLOW code modification. The original numerical model is simplified into a two-phase, gas and liquid flow model. Then non-linear flow mechanisms were incorporated into this two-phase flow simulator and a mesh generation program about horizontal wells and multi-stage hydraulic fractures reservoirs were developed for this simulator. This chapter presents brief information on model formulations, i.e., the mathematical and numerical implementation.

3.1 Flow Governing Equations

The two phase flow model, gas and water (or liquid), in a porous or fractured unconventional reservoir is assumed to be similar with what is described in the black oil model. It is composed only of two phases: gaseous and aqueous phases. For simplicity, the gas and water components are assumed to be present only in their associated phases and adsorbed gas is within the solid phase of rock. Each phase flows in response to pressure, gravitational, and capillary forces according to the multiphase extension of Darcy law or several extended non-Darcy flow laws, discussed below. In an isothermal system containing two mass components, subject to multiphase flow and adsorption, two mass-balance equations are needed to fully describe the system, as described in an

arbitrary flow region of a porous or fractured domain for flow of phase β (β = g for gas and β = w for water),

$$\frac{\partial}{\partial t}(\phi S_\beta \rho_\beta + m_g) = -\nabla \bullet (\rho_\beta \mathbf{v}_\beta) + q_\beta \qquad (3.1)$$

where ϕ is the effective porosity of porous or fractured media; S_β is the saturation of fluid β; ρ_β is the density of fluid β; $\mathbf{v}_\beta$ is the volumetric velocity vector of fluid β, determined by Darcy's law or non-Darcy's flow models, discussed in the below; t is time; m_g is the adsorption or desorption mass term for gas component per unit volume of rock formation; and $\mathbf{q}_\beta$ is the sink/source mass term of phase (component) β per unit volume of formation.

3.2 Constitutive Relations

The governing Equations (3.1) of mass conservation for the two phases need to be supplemented with constitutive equations, which express all the parameters as functions of a set of primary thermodynamic variables of interest. The following relationships will be used to complete the statement of describing multiple phase flow of gas and liquid through porous and fractured media.

- **Saturation Constraint**

$$S_w + S_g = 1 \qquad (3.2)$$

- **Capillary Pressure Functions**

$$P_w = P_g - P_{cgw}(S_w) \tag{3.3}$$

where P_{cgw} is the gas-water capillary pressure in a two-phase system, which is assumed to be a function of water or gas saturation only.

- **Relative Permeability Functions**

$$k_{rw} = k_{rw}(S_w) \tag{3.4}$$

$$k_{rg} = k_{rg}(S_g) \tag{3.5}$$

- **PVT Data**

$$\rho_w = \frac{(\rho_w)_{STC}}{B_w} \tag{3.6}$$

$$\rho_g = \frac{Z_g M_g P}{RT} \tag{3.7}$$

where B_β is formation volume factor for phase β; $(\rho_\beta)_{STC}$ is density of phase β at standard condition (or storage tank conditions); M_g is average molecular weight; Z_g is the z factor to calibrate gas density from ideal gas to real gas; R is universal gas constant.

- **Fluid Viscosities**

$$\mu_g = \mu_g(P_g) \tag{3.8}$$

- **Porosity of Formation**

$$\phi = \phi^{o}\left(1 + C_{r}\left(P - P^{o}\right) - C_{T}\left(T - T^{o}\right)\right) \qquad (3.9)$$

where ϕ^{o} is the effective porosity of formation at reference pressure of, P^{o}; and reference temperature, T^{o}; and C_T is thermal expansion coefficient of formation rock.

3.3 Time and Space Discretization

In this simulator, the mass conservation equations are discretized in space by the integral finite difference method (Pruess et at. 1999), as shown in Figure 3.1. Time discretization is carried out using a backward, first-order, fully implicit finite-difference scheme. The discrete nonlinear equations for mass conservation of gas and water at grid block or node i can be written in a general form:

$$\left\{\left(\phi S_{\beta}\rho_{\beta}\right)_{i}^{k,n+1} + m_{i}^{k,n+1} - \left(S_{\beta}\rho_{\beta}\right)_{i}^{k,n} - m_{i}^{k,n}\right\}\frac{V_i}{\Delta t} = \sum_{j\in\eta_i} flow_{ij}^{k,n+1} + Q_{i}^{k,n+1} \qquad (3.10)$$

(k = 1, 2) and (i=1, 2, 3, …, N)

where superscript k serves also as an equation index for gas and water mass components with k = 1 (gas) and 2 (water); superscript n denotes the previous time level, with n+1 the current time level to be solved; subscript i refers to the index of grid block or node I; with N being the total number of nodes in the grid; Δt is time step size; V_i is the volume of node i; η_i contains the set of direct neighboring nodes (j) of node i; m_i^k, $flow_{ij}^k$, and Q_i^k are the reaction (absorption or desorption) terms at node i; the component mass "flow"

term (or F_{ij} in Figure 3.1) between nodes i and j, and sink/source term at node i for component k, respectively, defined below:

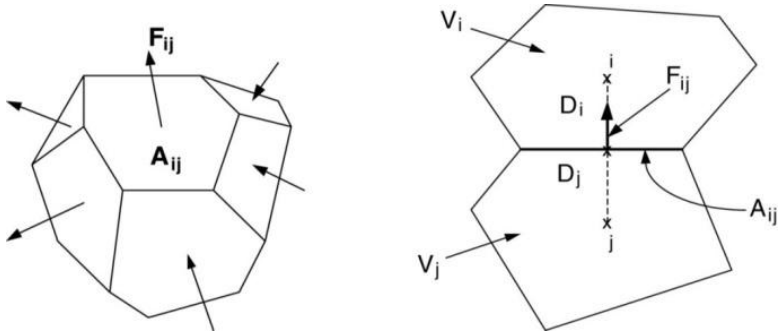

Figure 3.1 Space discretization and flow-term evaluation in the integral finite difference method (Pruess et al. 1999)

Based on the Darcy's law, the mass flux of fluid phase β along the connection in discrete mass conservation Equation (3.10) is given by

$$\text{flow}_{\beta,ij} = \lambda_{\beta,ij+1/2}\gamma_{ij}\left(\Phi_{\beta j} - \Phi_{\beta i}\right) \tag{3.11}$$

where $\lambda_{\beta,i\,j+1/2}$ is the mobility term to phase β, defined as

$$\lambda_{\beta,i\,j+1/2} = \left(\frac{\rho_\beta k_{r\beta}}{\mu_\beta}\right)_{ij+1/2} \tag{3.12}$$

In Equation (3.11), γ_{ij} is transmissibility. For a Voronoi grid, it is defined as (Pruess et al. 1999),

$$\gamma_{ij} = \frac{A_{ij}\,k_{i\,j+1/2}}{d_i + d_j} \tag{3.13}$$

where A_{ij} is the common interface area between the connected blocks or nodes i and j (Figure 3.1); d_i is the distance from the center of block i to the common interface of blocks i and j (Figure 3.1.1, note d_i is defined as D_i in Figure 3.1.1)); and $k_{ij+1/2}$ is an averaged (such as harmonic-weighted) absolute permeability along the connection between elements i and j.

3.4 Klinkenberg Effect

Klinkenberg effect mainly influences gas phase flow in the calculation. To incorporate the Klinkenberg effect which is mathematically expressed in Equation (2.1), one term is added in the mobility term to gas phase in Equation (3.12).

$$\lambda_{g,i\,j+1/2} = \left[\frac{\rho_g k_{rg}}{\mu_g} \left(1 + \frac{b}{P_g} \right) \right]_{ij+1/2} \tag{3.14}$$

The reason why the Klinkenberg effect is added in the mobility term instead of the transmissibility term is that Klinkenberg effect is pressure dependent. Its value will change with the change in block/node pressure. In MSFLOW, transmissibility term for each connection is only calculated once at the beginning and then these values are saved for the entire calculation. By contrast, the mobility term is changed with simulation going on for each iteration step.

Note for gas flow between two grid blocks: i and j, there are two permeability values calculated (ij+1/2), one for each block, therefore a proper weighting of the two absolute permeabilities. In this research project, an upstream weighting method is applied to get the average of these two permeabilities.

3.5 Non-Darcy Flow

Under the high-velocity, non-Darcy flow condition, if *Forchheimer* Equation (2.4) is selected to describe the high flow rates, the mass flow term ($\text{flow}_{\beta,ij}$) in Equation (3.11) along the connection (i, j), between grid blocks i and j, is numerically defined as (Wu, 2002),

$$\text{flow}_{\beta,ij} = \frac{A_{ij}}{2\left(k\beta_\beta\right)_{ij+1/2}}\left\{-\frac{1}{\lambda_\beta}+\left[\left(\frac{1}{\lambda_\beta}\right)^2-\bar{\gamma}_{ij}\left(\Phi_{\beta j}-\Phi_{\beta i}\right)\right]^{1/2}\right\} \qquad (3.15)$$

in which the non-Darcy flow transmissibility is defined as,

$$\bar{\gamma}_{ij} = \frac{4\left(k^2\rho_\beta\beta_\beta\right)_{ij+1/2}}{D_i + D_j} \qquad (3.16)$$

3.6 Gas Adsorption/Desorption

In this work, gas adsorption is treated as another source to store or release gas apart from the free gas in pores. As the pressure drops with continuous gas production from the reservoir, gases that are adsorbed on rocks desorb and contribute to the gas production. Thus for the accumulation term in gas phase mass-balance equation, apart from the original free gas accumulation in micro/macro pores, the adsorption part is added. Equation (3.1) shows that this model and the mass of adsorbed gas in unit formation volume is described as (Silin and Kneafsey, 2011; Wu et al. 2012):

$$m_g = \rho_R \rho_g V_E \qquad (3.17)$$

where m_g is absorbed gas mass in unit formation volume; ρ_R is rock bulk density; ρ_g is gas density at standard condition; and V_E is the adsorption isotherm function or gas content in scf/ton (or standard gas volume adsorbed per unit rock mass).

If the adsorbed gas terms can be represented by the Langmuir isotherm (Langmuir, 1916), the dependency of adsorbed gas volume on pressure at constant temperature is given below,

$$V_E = V_L \frac{P}{P + P_L} \tag{3.18}$$

where V_L is the Langmuir's volume in scf/ton; P is reservoir gas pressure; and P_L is Langmuir's pressure, the pressure at which 50% of the gas is desorbed. In general, Langmuir's volume V_L is a function of the organic richness (or TOC).

One issue needs to be mentioned is that adsorption item is added directly in the accumulation part. This mathematical expression indicates that with pressure changes, adsorbed gas on rocks will reach a balance with free gas in pores immediately. In other work, the gas transport process of gas desorption is neglected. Basically, this assumption is acceptable because of two considerations. First, rates of molecular diffusion and mass transport are not of the same magnitude and the former one is much higher than the latter one. Second, pressure in unconventional reservoirs changes slowly due to the extremely low reservoir permeability or low flow rate. So as the pressure changes, the time needed to reach a new balance between gas adsorbed and free gas is so short to be neglected.

3.7 Geomechanics Effect

A simple, fully coupled model presented in Section 2.1.4 is used to include the geomechanical effect on gas flow. If the stress field is predetermined as a function of spatial coordinates and fluid pressure, the effect of rock deformation on fluid flow can be evaluated using the equations in Section 2.1.4. To include the effect of geomechanics on rock deformation in an unconventional reservoir, it is important to determine those correlations, in particular, for porosity and permeability, such as Equations (2.7) and (2.8), as functions of mean effective stress from laboratory or field studies. The key procedure to incorporate the geomechanics effect is as follows:

1. Calculate effective stress or their changes at each Newton iteration as functions of pressure according to Equations (2.7) and (2.8)
2. Calculate updated mean effective stress
3. Calculate porosity, permeability, and capillary pressure using correlations, such as Equations (2.10), and (2.11) as functions of mean stress
4. Substitute the modified porosity, permeability, and capillary pressure values in calculation of the accumulation term and flow term in Equation (3.1).

Note that for a fully coupled flow-mechanics calculation, these calculations must be done at Newton-Raphson iteration level, not time-step level.

3.8 Equation of State (EOS) for Gas Phase

Equations (3.7) and (3.8) show the constitutive correlations that consider gas density and viscosity change with pressure and temperature. In the simulator, two

approaches are provided to handle this problem. The first one is inputting discrete data points that include information about Z factor and gas viscosity at different pressures. The simulator will linear-interpolate these points to get Z factor and gas viscosity value at the needed pressure. The second method is using theoretical derivation and closed-form correlation equations that the simulator will generate these data automatically once the gas component parameters are input.

3.8.1 Peng-Robinson Equation of State to Calculate Gas Composition Density

Peng-Robinson equation of state (Peng and Robinson, 1976) is a good approach for calculation of thermodynamic properties of one pure or mixture system.

$$p = \frac{RT}{V_m - b} - \frac{a}{V_m^2 + 2bV_m - b^2} \tag{3.19}$$

where

$$a = \sum_i \sum_j y_i y_j a_{ij} \tag{3.20}$$

$$b = \sum_i y_i b_i \tag{3.21}$$

$$a_{ij} = (1 - \delta_{ij})\sqrt{a_i a_j}\,(i \neq j) \tag{3.22}$$

$$a_{ii} = a_i \tag{3.23}$$

$$a_i = \frac{0.45724 R^2 T_{ci}^2}{P_{ci}} \left[1 + \kappa_i \left(1 - \sqrt{\frac{T}{T_{ci}}} \right) \right]^2 \tag{3.24}$$

$$\kappa_i = 0.37464 + 1.54266w_i - 0.26992w_i^2 \tag{3.25}$$

$$b_i = \frac{0.07780RT_{ci}}{P_{ci}} \tag{3.26}$$

In the above formulations, T_{ci} , P_{ci}, w_i is the critical temperature, critical pressure and acentric factor for a certain component. So once the pressure and temperature of the system are given, we could calculate the mole volume, Z factor and gas density.

3.8.2 Lee, Gonzalez, and Eakin, Correlation for Gas Viscosity

The Lee correlation (Lee, et al., 1966) evolved from the existing work in the estimation of hydrocarbon gas viscosity using temperature, gas density at a specific temperature and pressure, and the molecular weight of the gas. The correlation is given by:

$$\mu_g = 10^{-4} K \exp(X\rho^Y) \tag{3.27}$$

where:

$$K = \frac{(9.379 + 0.01607M_w)T^{1.5}}{209.2 + 19.26M_w + T} \tag{3.28}$$

$$X = 3.448 + \left[\frac{986.4}{T}\right] + 0.01009M_w \tag{3.29}$$

$$Y = 2.447 - 0.2224X \tag{3.30}$$

and, ρ = Density at temperature and pressure, g/cc

M_w = Molecular weight of gas mixture, lb/lb-mole

T = Temperature, ^oR

μ_g = Gas viscosity at temperature and pressure, cp

3.9 Fracture Conceptual Models

In our opinion, the hybrid-fracture modeling approach, defined as a combination of explicit-fracture (discrete fracture model), MINC (Pruess and Narasimham, 1985), and single-porosity modeling approaches, seems the best option for modeling a shale gas reservoir with both hydraulic fractures and natural fractures. This is because hydraulic fractures, which have to be dealt with for shale gas production, are better handled by the explicit fracture method, and they cannot be modeled in general by a dual-continuum model. On the other hand, natural fractured reservoirs are better modeled by a dual-continuum approach, such as MINC for extremely low-permeability matrix and long lasting transient flow in shale gas formations, which cannot be modeled by an explicit fracture or classic double-porosity model.

Explicit fracture or discrete fracture concept is explicitly to include every fracture in the modeled system using refined grids to discretize fractures and the matrix surrounding fractures. This approach is a good option for simulating hydraulic fractures for gas production from hydraulic fractured wells in a non-fractured shale gas reservoir. The advantage of this approach is that it can model hydraulic fractures accurately when the fractures are known for their spatial distributions, determined from other fracture

characterization studies. The disadvantage is that it cannot be used for simulating natural fractures or micro fractures in general, because the number of natural or micro fractures in a shale gas reservoir is too large for the model to handle and spatial distributions are unknown.

For the low matrix permeability or large matrix block size, the traditional double-porosity model may not be applicable for modeling natural fractures in unconventional reservoirs. This is because it takes years to reach the pseudo-steady state under which the double-porosity model applies. The MINC concept (Pruess and Narasimham, 1985) is able to describe gradients of pressures, temperatures, or concentrations near matrix surface and inside the matrix–by further subdividing individual matrix blocks with one- or multidimensional strings of nested meshes. Therefore, the MINC method treats interporosity flow in a fully transient manner by computing the gradients which drive interporosity flow at the matrix-fracture interface. In comparison with the double-porosity or dual-permeability model, MINC does not rely on the pseudo-steady state assumption to calculate fracture-matrix flow and is able to simulate fully transient fracture-matrix interaction by subdividing nested-cell gridding inside matrix blocks. The MINC concept should be generally applicable for handling fracture-matrix flow in fractured shale gas reservoirs, no matter how large the matrix block size is or how low the matrix permeability is and is more suitable for handling fractured shale gas reservoirs. However, the MINC approach may not be applicable to systems in which fracturing is so sparse that the fractures cannot be approximated as a continuum.

As Figure 3.2 shows, in this hybrid-fracture model, both the hydraulic fractures and SRV are evaluated from the microseismic cloud. Recent progresses in microseismic

fracture mapping technology provide some useful information to characterize hydraulic fracture growth, stimulated reservoir volume. It documents surprising complexities in many geological environments. Based on the available microseismic data, a primary hydraulic fracture and its associated stimulated volume in each stage can be built. The primary fractures are defined first with the orientation and region of the microseismic clouds. These hydraulic fractures are modeled by discrete fracture method. Relevant stimulated reservoir volumes (SRV) near the hydraulic fractures are assumed to be natural-fractured and MINC is applied in this area. Single-porosity is applied in the region outside the SRV. Local grid refinement (LGR) can improve simulation accuracy because pressure gradients change substantially over short distances in the regions near hydraulic fractures. LGR is performed near the hydraulic fracture region.

3.10 Pseudo Pressure Considering Klinkenberg Effect and Adsorption

In 1965, Al-Hussainy and Ramey derived the pseudo pressure which has been since used successfully to analyze the flow of real gases.

$$m(P) = 2\int_{P_0}^{P} \frac{P'}{\mu Z} dP' \qquad (3.31)$$

where P_0 is reference pressure; P is gas pressure; μ is the gas viscosity; and Z is real gas Z factor.

The concept of the real gas pseudo-pressure promises a considerable simplification and improvement in all phases of gas well analysis and gas reservoir calculations. These analysis and calculations may work well for the conventional

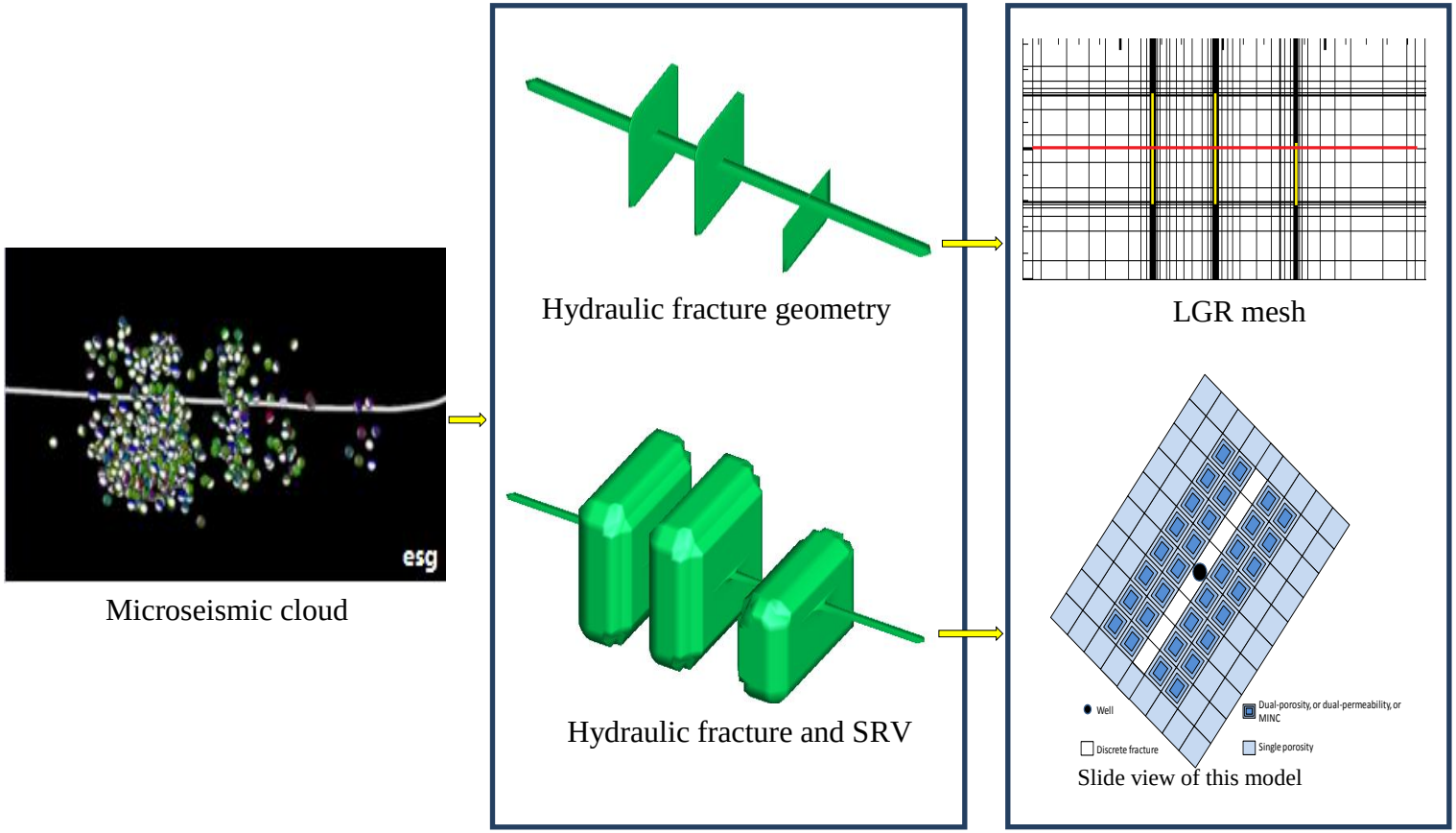

Figure 3.2 Hybrid-fracture model built methodology from micro-seismic cloud

reservoirs but could have some trouble when used directly in the unconventional reservoirs analysis. This is because gas flow in ultra-low permeability unconventional reservoirs is subject to more nonlinear, coupled processes, including nonlinear adsorption/desorption, non-Darcy flow (at high flow rate and low flow rate), and strong rock-fluid interaction, and rock deformation within nanopores or micro-fractures, coexisting with complex flow geometry and multi-scaled heterogeneity.

In appendix A, we give the gas pseudo-pressure derivation considering Klinkenberg effect and gas adsorption.

$$m(P) = 2\int_{P_0}^{P} \frac{P'(1+b/P)}{\mu(P)Z(P)} dP' \tag{3.32}$$

In the formulation derivation, we find that gas adsorption part in the accumulative item can be equivalently treated as a pressure-depended compressibility factor, similar with the traditional free gas compressibility:

$$c_a(P) = \frac{Z(P)}{P} \frac{RT\rho_K\rho_g V_L P_L}{\phi M\left(P+P_L\right)^2} \tag{3.33}$$

Below an estimation of "free gas compressibility" and "adsorption compressibility" with pressure are calculated from Equations (3.32) and (3.33). Calculation parameters are shown below in Figure 3.3 and Table 3.1.

Figure 3.4 is the calculated adsorption compressibility value and this value is in the same magnitude with the rock and fluids total compressibility. These results suggest when the pressure increase from 2000psi to 5000psi, this compressibility drops from 2.71×10^{-4}/psi to 4.29×10^{-5}/psi.

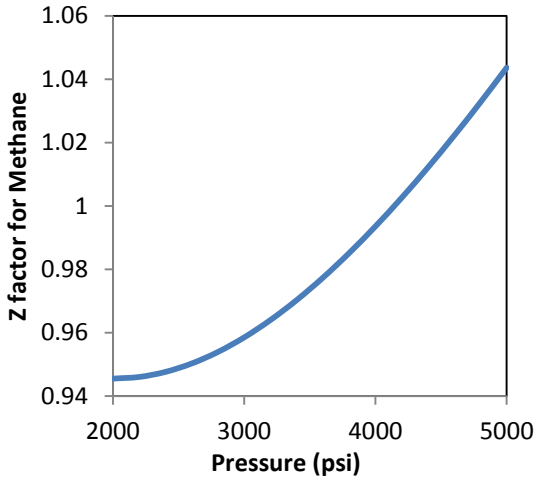

Figure 3.3 Methane Z factor at 122 0F from 2000 to 5000 psi

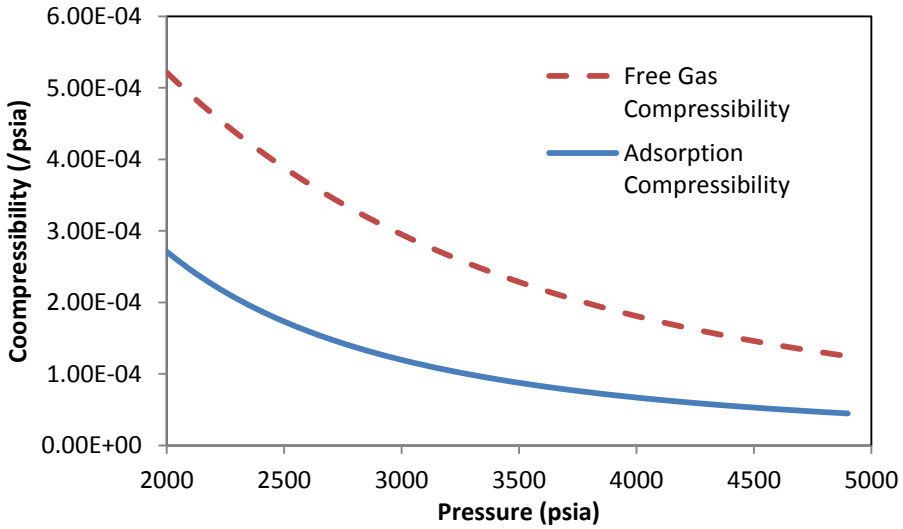

Figure 3.4 Free gas compressibility and adsorption compressibility vs. pressure

Table 3.1 Data for “free gas compressibility” and "adsorption compressibility"

Parameters	Value	Units
Gas type	Methane	
Porosity, ϕ	0.05	
Temperature, T	122	F
Rock density, ρ_K	2.7	g/cc
Langmuir’s volume, V_L	218.57	Scf/ton
Langmuir’s pressure, P_L	2285.7	psi

CHAPTER 4

MODEL VERIFICATION AND VALICATION

To achieve the goal of developing an accurate and credible simulation model, model verification and validation need to be done. In this chapter, a series of verification cases are presented. Analytical solution results, experimental data from National Institute of Standards and Technology (NIST), and well testing curves are used for model verification and validation efforts.

4.1 Gas Viscosity and Density Calculation

The viscosity and density functions of single component or multicomponent real gases are added in the simulator EOS module. This provides users another approach in addition to viscosity and density input in table look up, as mentioned in section 3.8. In this module, several gas properties, such as critical temperature, critical pressure, acentric factor, and binary interaction parameters are included in the simulator. These properties are shown in Table 4.1 and 4.2. Once the mole fraction for each component and the system temperature are input, gas density and viscosity at a specific pressure will be calculated in this program and be used for the subsequent calculation.

This module is verified by comparing the calculated results with the experimental data from National Institute of Standards and Technology (NIST, a federal technology agency that works with industry to develop and apply technology, measurements and standards). First, the property of pure methane gas is tested and then for the mixture.

Figure 4.1 and Figure 4.2 show methane density and viscosity comparisons between calculated results and NIST data, which indicate the theoretical approach adopted in the simulator is acceptable.

Table 4.1 Properties of gas in the simulator

Name	Tc(K)	Pc(Mpa)	acentric factor
Methane	190.56	4.599	0.0115
Ethane	305.32	4.872	0.0995
Propane	369.83	4.248	0.1523
Butanes	425.12	3.769	0.2002
Pentanes	469.7	3.370	0.2515
Hexanes	507.6	3.025	0.3013
Heptanes	540.2	2.740	0.3495
Octanes	568.7	2.490	0.3996
Nonanes	594.6	2.290	0.4435
Decanes	617.7	2.110	0.4923
n-C12	658.0	1.820	0.5764
n-C15	708	1.480	0.6863
n-C20	768	1.160	0.9069
CO2	304.19	7.382	0.2280

Table 4.2 Binary interaction parameters table

BIP	CO2	Methane	Ethane	Propane	Butanes	Pentanes	Hexanes	Heptanes	Octanes	Nonanes	Decanes	n-C12	n-C15	n-C20
CO2	0.000	0.107	0.132	0.124	0.133	0.140	0.145	0.145	0.140	0.015	0.015	0.015	0.015	0.015
Methane	0.107	0.000	0.003	0.014	0.013	0.024	0.042	0.035	0.047	0.047	0.050	0.050	0.060	0.070
Ethane	0.132	0.003	0.000	0.001	0.010	0.008	0.014	0.015	0.016	0.019	0.030	0.030	0.040	0.050
Propane	0.124	0.014	0.001	0.000	0.003	0.012	0.027	0.056	0.059	0.007	0.020	0.020	0.025	0.030
Butanes	0.133	0.013	0.010	0.003	0.000	0.017	0.017	0.019	0.012	0.010	0.001	0.001	0.001	0.001
Pentanes	0.140	0.024	0.008	0.012	0.017	0.000	0.000	0.000	0.000	0.000	0.000	0.000	0.000	0.000
Hexanes	0.145	0.042	0.014	0.027	0.017	0.000	0.000	0.000	0.000	0.000	0.000	0.000	0.000	0.000
Heptanes	0.145	0.035	0.015	0.056	0.019	0.000	0.000	0.000	0.000	0.000	0.000	0.000	0.000	0.000
Octanes	0.140	0.047	0.016	0.059	0.012	0.000	0.000	0.000	0.000	0.000	0.000	0.000	0.000	0.000
Nonanes	0.015	0.047	0.019	0.007	0.010	0.000	0.000	0.000	0.000	0.000	0.000	0.000	0.000	0.000
Decanes	0.015	0.050	0.030	0.020	0.001	0.000	0.000	0.000	0.000	0.000	0.000	0.000	0.000	0.000
n-C12	0.015	0.050	0.030	0.020	0.001	0.000	0.000	0.000	0.000	0.000	0.000	0.000	0.000	0.000
n-C15	0.015	0.060	0.040	0.025	0.001	0.000	0.000	0.000	0.000	0.000	0.000	0.000	0.000	0.000
n-C20	0.015	0.070	0.050	0.030	0.001	0.000	0.000	0.000	0.000	0.000	0.000	0.000	0.000	0.000

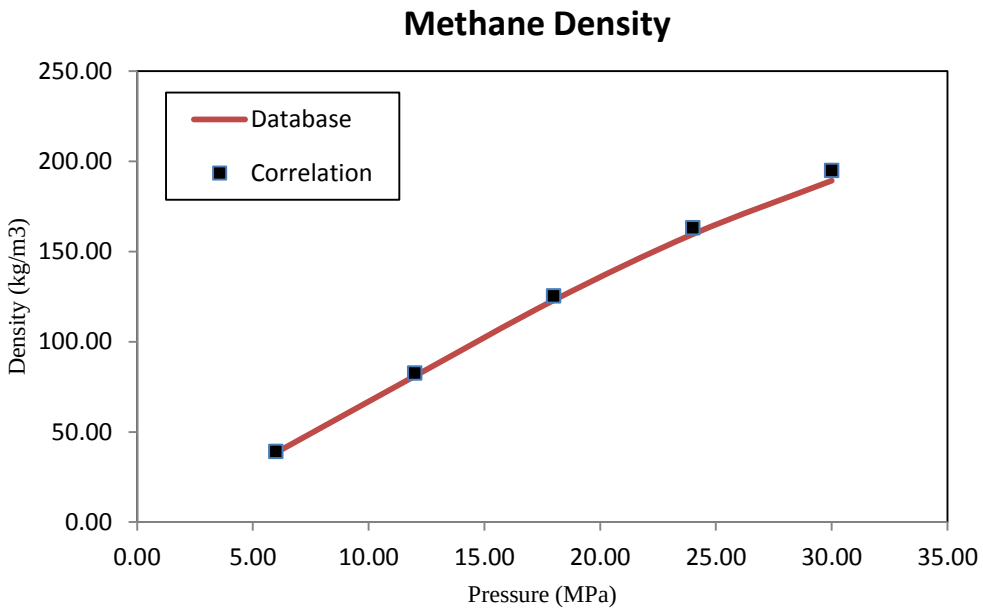

Figure 4.1 Methane density comparisons between MSFLOW-UG and NIST database

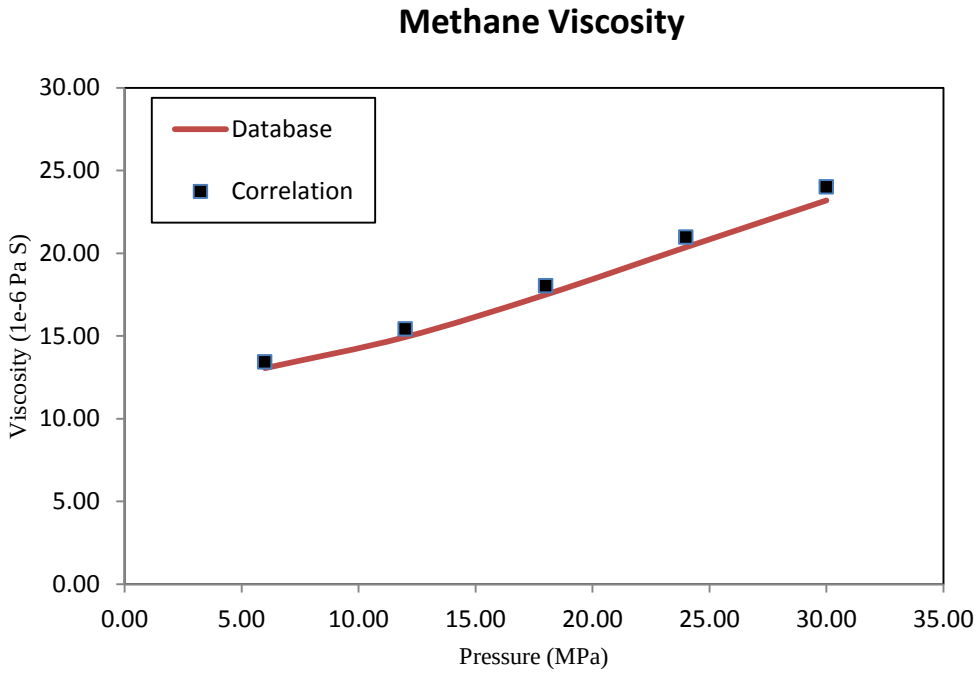

Figure 4.2 Methane viscosity comparisons between MSFLOW and NIST database

Calculated properties of natural gas and pure methane are also compared as shown in Figure 4.3 and 4.4. Natural gas composition is shown in Table 4.3.

Table 4.3 Natural gas composition

Natural Gas	
C1	94.92%
C2	2.50%
C3	0.20%
C4	0.06%
C5	0.02%
N2	1.60%
CO2	0.70%

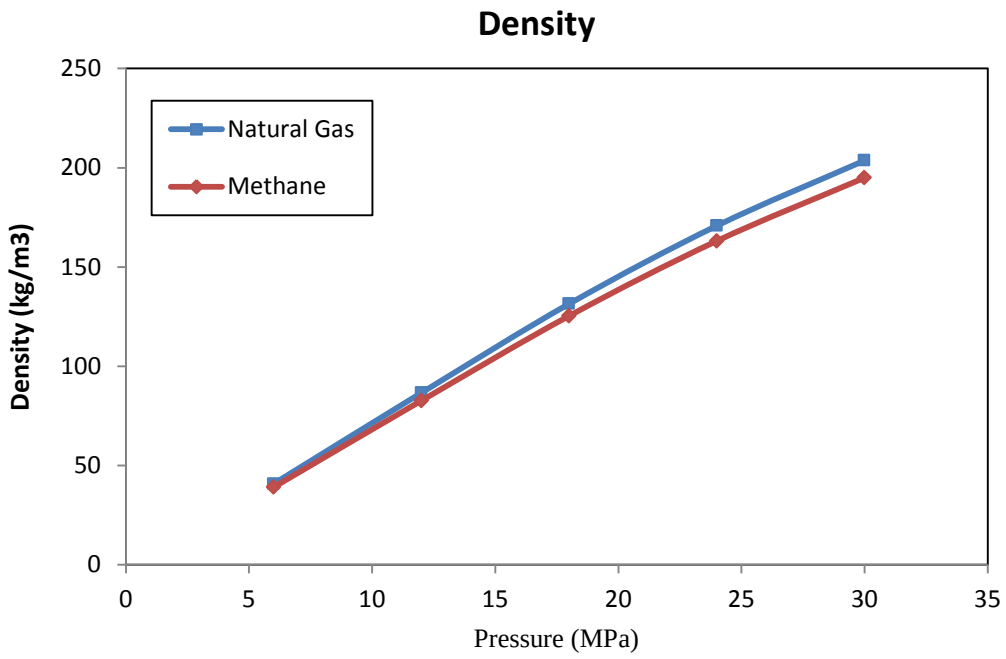

Figure 4.3 Density comparisons between natural gas and methane

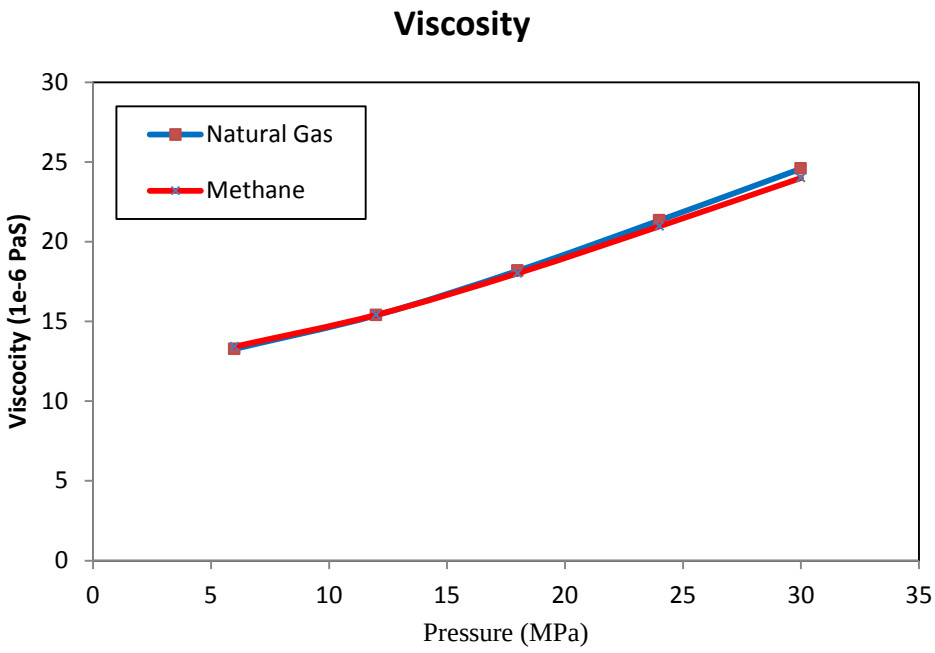

Figure 4.4 Viscosity comparisons between natural gas and methane

4.2 Semi-Log Straight Line Approach for Estimating Formation Permeability

This case is designed to test the equation of state for gas and pseudo-pressure codes in MSFLOW. Pressure drawdown testing is adopted here. In this scenario, gas is produced by one vertical well with constant rate in an infinite reservoir. The input details are shown below in Table 4.4.

Pseudo-pressure (i.e., pseudo gas pressure, known as real gas potential) is used for the transient well testing analysis of unconventional gas wells. It is defined as,

$$m(P) = 2\int_{P_0}^{P} \frac{P'}{\mu Z} dP' \qquad (4.1)$$

Gas pressure-viscosity, gas pressure-Z factor, and gas pressure-gas density relationships, as used in this study, are shown, in which the methane gas properties are used.

Dimensionless pseudo-pressure is defined as:

$$m_D = \frac{T_{sc} kh}{Q_{sc} T P_{sc}} \left[m(P_i) - m(P) \right] \tag{4.2}$$

Table 4.4 Calculation data for semi-log straight line analysis

Parameter	Value	Unit
matrix porosity	$\phi_m = 0.15$	
formation temperature	$T = 50$	℃
permeability	$k = 9.87 \times 10^{-17}$	m^2
reservoir radius	$r_e = 3{,}000$	m
reservoir thickness	$h = 10$	m
well radius	$r_w = 0.1$	m
initial reservoir pressure	$P_i = 2.07 \times 10^7$	Pa
initial gas saturation	$S_{gi} = 0.98$	
gas production rate	$Q_g = 1.0 \times 10^3$	m^3/day
skin factor	$S = 0$	
gas viscosity	$\mu = 1.84 \times 10^{-5}$	PaS

Based on the well-testing study, semi-log scope determined from the figure provides an approach to estimate the formation permeability (note that units in the calculation are converted to SI), as follows:

$$m = 4.72 \times 10^{17} \left(\frac{Pa}{s} \right) = 0.993 \times 10^{7} \left(\frac{psi^2}{cp} \right) \tag{4.3}$$

$$P_{sc} = 14.7 psi \tag{4.4}$$

$$h = 10m = 32.81 ft \tag{4.5}$$

$$q_{sc} = 1000 \frac{m^3}{day} = 35.3147 \frac{Mscf}{day} \tag{4.6}$$

$$T_{sc} = 520 R \tag{4.7}$$

$$T = 50^{o} C = 572 R \tag{4.8}$$

$$K = \frac{57898 q_{sc} P_{sc} T}{|m| h T_{sc}} = 0.1032 md \tag{4.9}$$

The actual value of permeability used in the numerical well testing is 0.1md. Considering some approximation in the pseudo-pressure definition, difference between them is ignorable. This match indicates the accuracy of handling state equation and pseudo-pressure.

4.3 Klinkenberg Effect

This is to examine the accuracy of our simulator formulation in simulating porous medium gas flow with the Klinkenberg effect. The problem concerns steady-state gas flow across a rock. Linear flow system is considered in this example as shown in Figure 4.6.

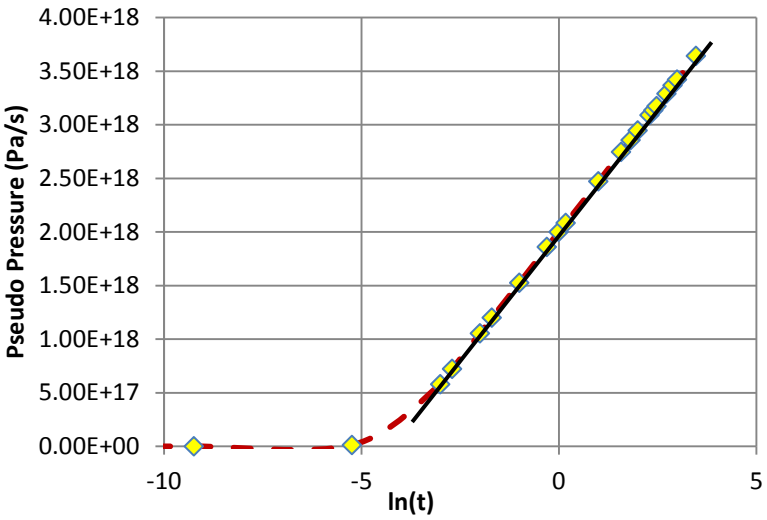

Figure 4.5 Numerical well testing curves to determine reservoir permeability for verification

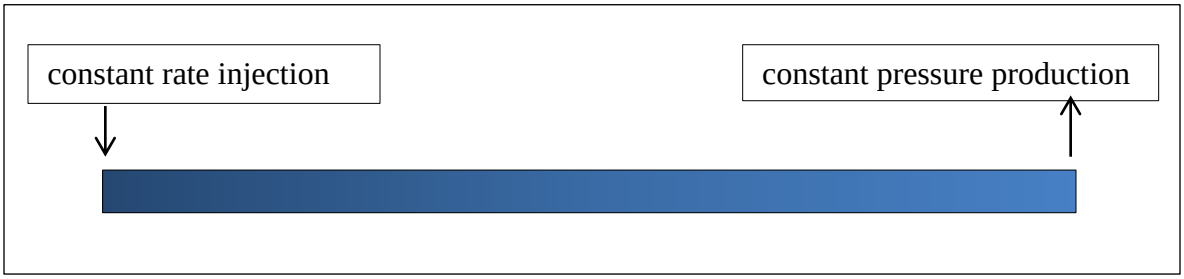

Figure 4.6 Linear flow model for verification of Klinkenberg effect

The system remains at steady-state gas flow at an isothermal condition, and a constant gas mass injection/production rate is imposed at one side of the rock. The other side of the rock is kept at a constant pressure. Eventually, the system will reach steady state. A comparison of the pressure profile along the rock block from the simulation and the exact, analytical solution is shown above, indicating that our simulated pressure distribution is in excellent agreement with the analytical solution for these problems.

Parameter details for this example are in Table 4.5. The analytical solution is included in the paper SPE 154448 and shown below (Wu, 2012). Details about this solution derivation are also presented in Appendix B.

Table 4.5 Calculation data for gas flow with Klinkenberg effects verification

Parameter	Value	Unit
Porosity	$\Phi = 0.3$	
Permeability	$k_\infty = 5 \times 10^{-19}$	m^2
klinkenberg coefficient	$b = 7.6 \times 10^6$	Pa
compressibility factor	$\alpha = 5.985 \times 10^{-6}$	$kg/Pa\ m^3$
gas viscosity	$\mu = 1.84 \times 10^{-5}$	Pa s
formation temperature	$T = 50$	℃
gas mass injection rate	$Q_m = 1 \times 10^{-6}$	kg/s
outlet boundary pressure	$P_L = 1 \times 10^5$	Pa
cross-area	A=1	m^2
model height	H=1	m

Simulations about this example are also carried out to have a comparison with the analytical result. To guarantee the system reach steady state, the total running time for this case is very long about 10^8 days. Figure 4.7 shows the comparison between the analytical results and numerical results, which indicate the formulation in the simulator about Klinkenberg effect is accurate and applicable.

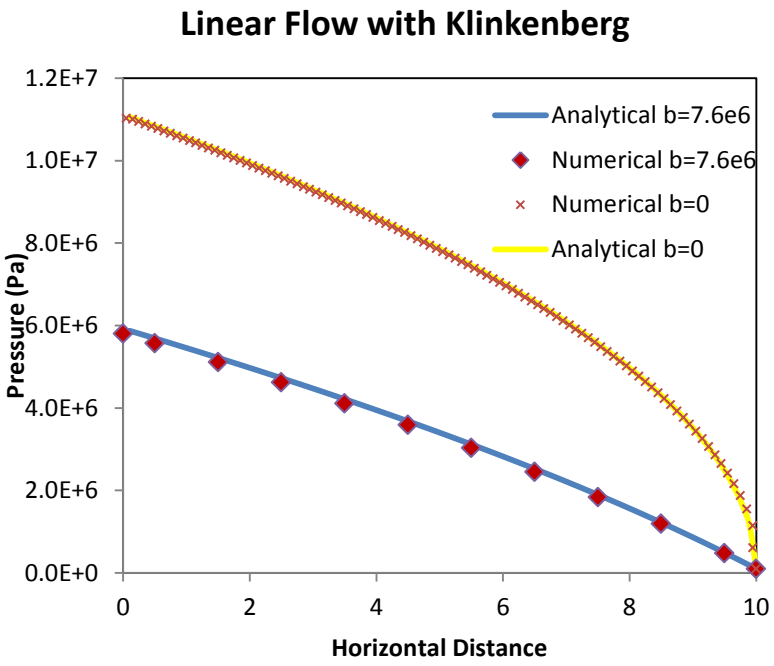

Figure 4.7 Numerical and analytical results comparison with Klinkenberg effect

4.4 Non-Darcy Flow

This is to examine the accuracy of our simulator formulation in simulating porous medium gas flow with non-Darcy flow. The problem concerns steady-state gas flow across a rock. Linear flow is considered in this example. The system contains steady-state gas flow at an isothermal condition, and a constant gas mass injection/production rate is imposed at one side of the rock. The other side of the rock is kept at a constant pressure. Eventually, the system will reach steady state. A comparison of the pressure profile along the rock block from the simulation and the exact, analytical solution is shown above, indicating that our simulated pressure distribution is in excellent agreement with the analytical solution for these problems. The analytical solution is included in the paper

SPE 154448 (Wu et al., 2012). Details about this solution derivation are also presented in Appendix C.

Simulation work about this example with the parameters in Table 4.6 is also done to have a comparison with the analytical result. To guarantee the system reach steady state, total running time for this case is very long about 10^8 days. Figure 4.8 shows the comparison between the analytical results and numerical results, which indicate the formulation in the simulator about non-Darcy flow is accurate and applicable.

Table 4.6 Calculation data in problem for gas non-Darcy flow verification

Parameter	Value	Unit
Porosity	$\Phi = 0.3$	
Permeability	$k_\infty = 5 \times 10^{-19}$	m^2
compressibility factor	$\alpha = 1.18 \times 10^{-5}$	$kg/Pa\ m^3$
gas viscosity	$\mu = 1.84 \times 10^{-5}$	Pa s
formation temperature	$T = 50$	℃
gas mass injection rate	$Q_m = 1 \times 10^{-6}$	kg/s
outlet boundary pressure	$P_L = 1 \times 10^5$	Pa
cross-area	A=1	m^2
model height	H=1	m
non-Darcy flow constant	$c_\beta = 0$	$m^{1.5}$
	$c_\beta = 1.0 \times 10^{-3}$	
	$c_\beta = 1.0 \times 10^{-4}$	

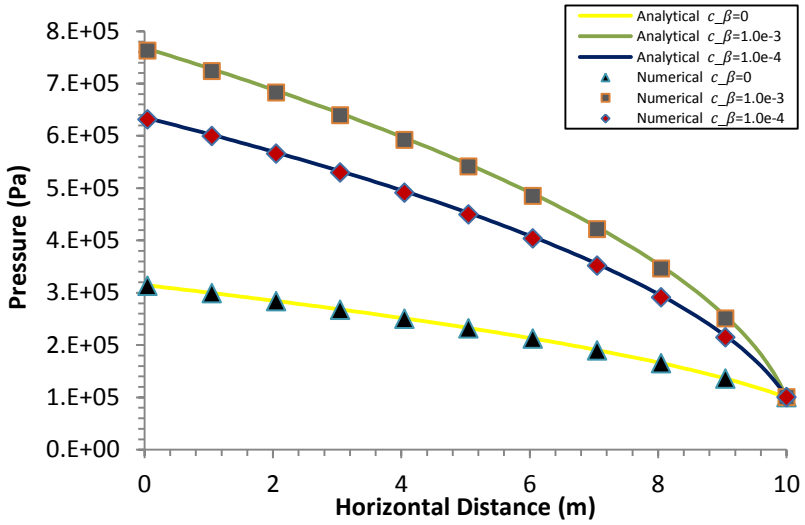

Figure 4.8 Analytical and Numerical Results for Non-Darcy Gas Flow

4.5 Adsorption Effect

For gas flow with adsorption, the transient analytical solution is given in Appendix D. It considers gas production from a vertical well in an infinite reservoir with one dimensional radial flow. Appendix D gives the details about this derivation.

The parameters used for this comparison study are: porosity $\Phi = 0.15$; permeability k = 100 mD; formation temperature $T = 25^{o}C$; gas viscosity $\mu = 1.64 \times 10^{-2}$cp ; initial pressure $P_i = 10^5$Pa and thickness of the radial system is 1m. The well boundary condition is: air mass injection rate: $Q = 1.0 \times 10^{-4}$kg/s.

Figure 4.9 presents the comparisons of the pressure profile at 1.16 days from the numerical and analytical solutions. Two situations, Langmuir volume $V_L = 0$ and $V_L = 50\ m^3/kg$, are considered. The analytical solutions give excellent match with numerical solution.

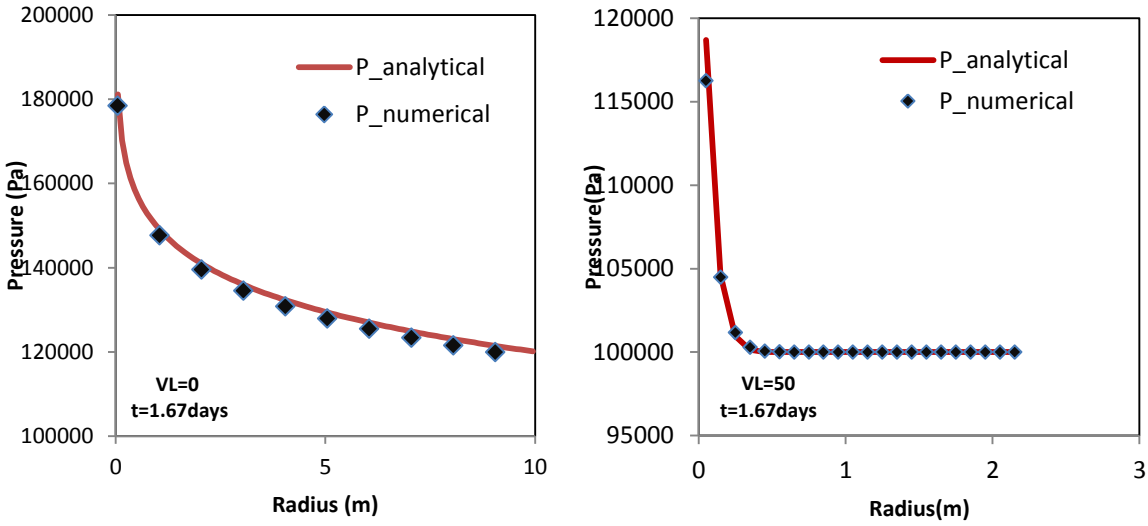

Figure 4.9 Comparison of gas pressure profiles considering gas adsorption in a radial system at 1.67 days, calculated using the numerical and analytical solutions

4.6 Geomechanics Effect

Wu and Pruess (2000) presented an analytical method for analyzing the non-linear coupled rock permeability variation and fluid flow problem. Approximate analytical solutions for one-dimensional linear and radial flow are obtained by an integral method, which is widely used in the study of steady and unsteady heat conduction problems. The accuracy of integral solutions is generally acceptable for engineering applications. When applied to fluid flow problems in porous media, the integral method consists of assuming a pressure profile in the pressure-disturbance zone and determining the coefficients of the profile by making use of the integral mass balance equation.

Their flow system of interest is a semi-infinite linear reservoir. This reservoir is fully saturated with a single-phase fluid and then the same fluid is injected at a given

constant rate at one side. According to Wu and Pruess (2000), the integral solution for the pressure distribution in this zone is:

$$P(x,t) = P_i + \frac{\delta(t)}{3}\left[\frac{q_m \mu}{A\rho(P_o)k(P_o)}\right]\left[1-\frac{x}{\delta(t)}\right]^3 \tag{4.10}$$

where $\delta(t)$ is the pressure penetration distance. By substitute the functions of density and porosity and performing integration, the pressure penetration distance is given as:

$$\delta(t) = \left[\frac{12\rho(P_0)k(P_0)t}{\rho_i \phi_i C_t \mu}\right]^{1/2} \tag{4.11}$$

Table 4.7 Parameters for checking integral solution for flow with geomechanics effect

Parameter	Value	Unit
Initial pressure	$P_i = 10^7$	Pa
Initial porosity	$\Phi_i = 0.20$	
Initial fluid density	$\rho_w = 975.9$	kg/m^3
Cross-section area	A=1.0	m^2
Formation thickness	h=1.0	m
Fluid viscosity	$\mu = 0.35132 \times 10^{-3}$	$Pa \cdot s$
Fluid compressibility	$C_f = 4.556 \times 10^{-10}$	Pa^{-1}
Rock compressibility	$C_r = 5.0 \times 10^{-9}$	Pa^{-1}
Initial permeability	$k_0 = 9.860 \times 10^{-13}$	m^2
Water injection rate	$q_m = 0.01$	kg/s
Hydraulic radius	$r_w = 0.1$	m
Exponential index	c=2.22	

The parameters as shown in Table 4.7 are used to evaluate both the numerical solution and the integral solution. A comparison of injection and the exact numerical solutions is shown in Figure 4.10. The agreement between the two solutions is excellent for the entire transient period.

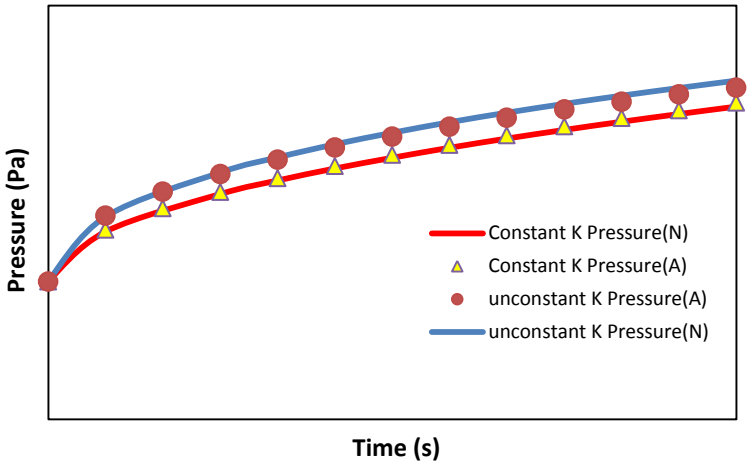

Figure 4.10 Comparison of injection pressures calculated from integral and numerical solutions for linear flow in a permeability-dependent medium with constant and inconstant permeability function

CHAPTER 5

MODEL APPLICATION

This chapter presents three application examples as follows:

1) We conduct a study of the "hydraulic fracture-matrix" linear flow and propose a methodology to estimate the total hydraulic fracture and matrix contact area.
2) We evaluate each of the above-mentioned non-linear flow mechanisms in a horizontal well, multi-stage hydraulic fractures reservoir scenario to see their influence on production.
3) We complete a history matching of field data.

These examples demonstrate the applicability of the reservoir simulator to modeling unconventional gas reservoirs.

5.1 Characterizing Hydraulic Fractures Using Transient Pressure Tests

This example presents applications of the unconventional reservoir simulator to quantify hydraulic fractures in shale gas reservoirs using transient pressure data. Modeling studies in this part indicate that the most sensitive parameter of hydraulic fractures to early transient gas flow through extremely low permeability rock is actually the fracture-matrix contacting area, generated by fracturing stimulation. Based on this observation, it is possible to use transient pressure testing data to estimate the area of

fractures generated from fracturing operations. We will conduct a series of modeling studies and present a methodology using typical transient pressure responses, simulated by the numerical model, to estimate fracture areas created or to quantity hydraulic fractures with traditional well testing technology. The type curves of pressure transients from this study can be used for quantify hydraulic fractures in field application.

The primary flow regime observed in a fractured tight/shale gas well is approximated as linear flow, which may continue for several years. Wattenbarger et al. (1998) gave the "short-term" approximations for this linear flow with constant rate, respectively,

$$m_{Di} - m_{Dwf} = \frac{200.8 T q_g B}{\sqrt{(\phi \mu c_t)_i}\sqrt{k}A}\sqrt{t} \qquad (5.1)$$

In Equation (5.1), m_D is the pseudo pressure; q_g is the gas rate; B is the gas formation volume factor; ϕ is the formation porosity; c_t is the total compressibility, k is the formation permeability; A is the hydraulic fracture area and t is the time; subscript i refers to initial condition and subscript wf refers to the wellbore condition;

Equation (5.1) indicates that for the constant-flowing-rate boundary condition, linear flow is characterized by a straight line on the plot of normalized pressure vs. the square root of time. The slope of this square-root-of-time plot provides some useful information for estimate the hydraulic fracture area. The accuracy of this estimation is influenced by initial pressure, formation average permeability and total compressibility. (Nobakht and Clarkson, 2012).

Below is a detailed discussion of this linear flow model, based on the simulation. First 3 fracture models with different fracture numbers, shapes but the same fracture-matrix contacting areas are simulated. Results show that the most sensitive parameter of hydraulic fractures to early transient gas flow through extremely low permeability rock is actually the fracture-matrix contacting area, generated by fracturing stimulation. Then gas adsorption phenomena and natural fracture systems around the hydraulic fracture are also studied on this model.

5.1.1 Different Fracture Numbers and Shapes

Figure 5.1 (a,b,c) are two-dimensional sketches for the three models mentioned above. In these figures, black lines represent the hydraulic fractures in the reservoir of size of $100\text{m} \times 100\text{m} \times 10\text{m}$. Horizontal wells are shown in these figures as well. But it ignores flow between reservoirs and horizontal wells. Only the flow from hydraulic fractures supports well production.

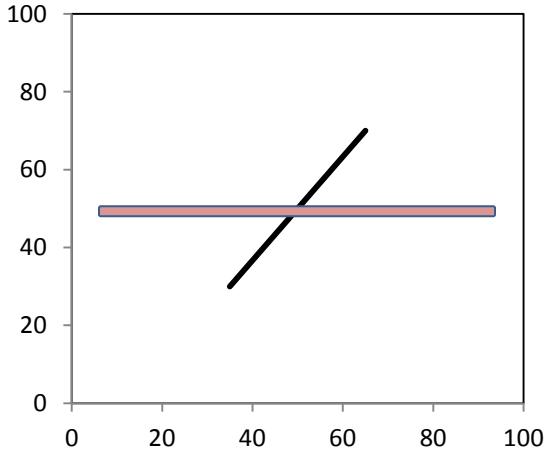

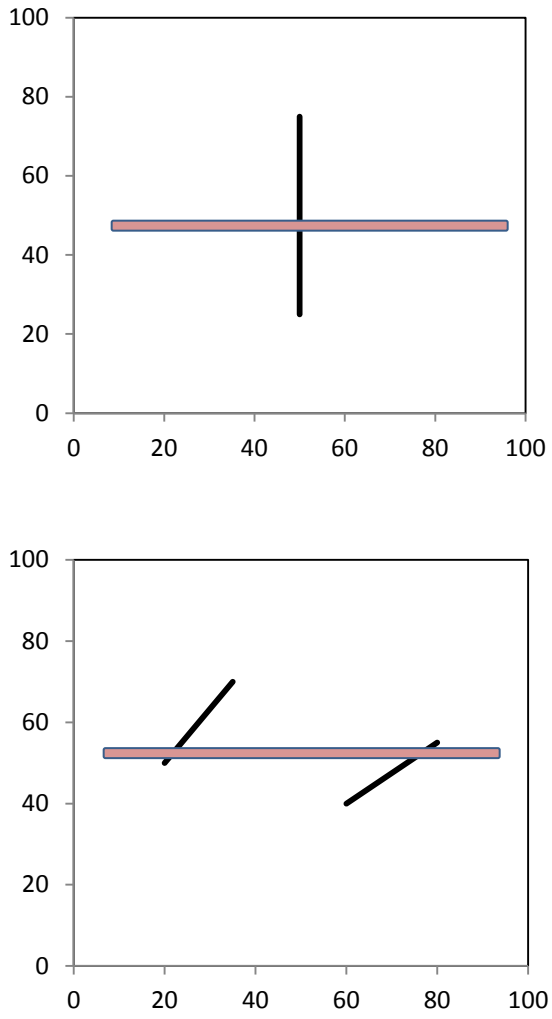

Figure 5.1 (a) Single hydraulic fracture diagonal to XY direction; (b) Single hydraulic fracture othogonal to XY direction; (c) Two hydraulic fractures diagonal to XY direction

Figure 5.2, 5.3 and 5.4 show the grids generated for the above three models. Units for X and Y coordinates in these figures are meters. A corse grid system is built with rectangular grids at initial and local grids refinement technology is then applied to better describe the area near hydraulic fractures. Grids that intersect with hydraulic fractures are continuely refined until the grid sizes are small enough to be in the same order of magnitude with fracture width. This grid-refining process enables us to accurately

describe flow characteristics near the hydraulic fracture region and gurantee the efficiency and accuracy of simulation results.

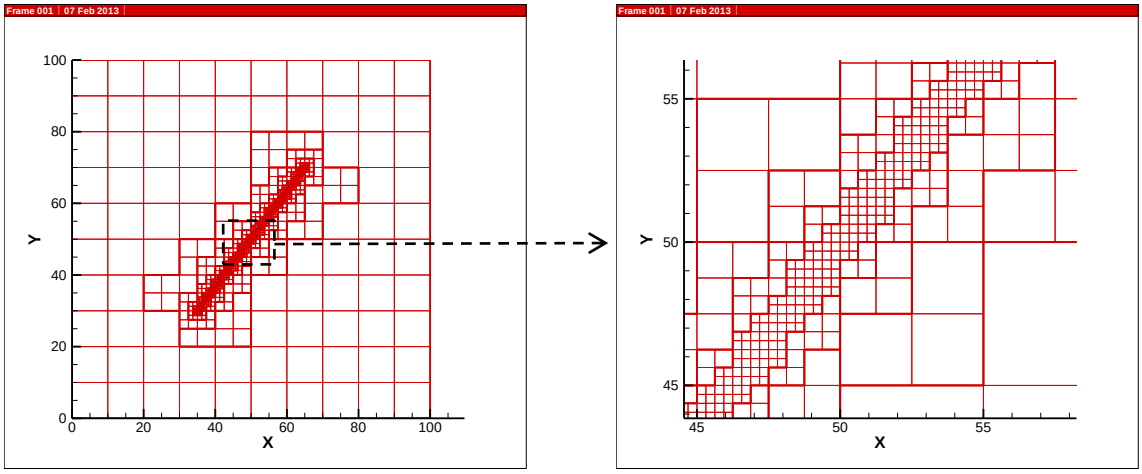

Figure 5.2 (a) Refine grids for Figure 5.1(a); (b) Local zoom in for Figure 5.1(a)

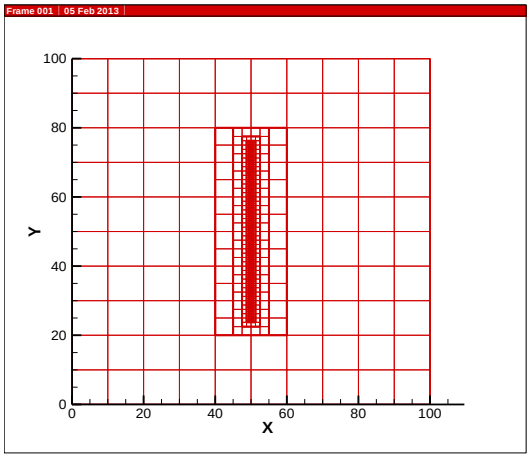

Figure 5.3 Refine grids for Figure 5.1(b)

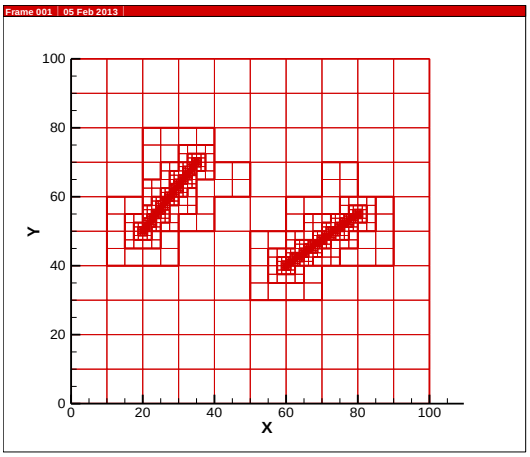

Figure 5.4 4 Refine grids for Figure 5.1(c)

Table 5.1 Input parameters for simulating the above three models

Parameters	Value	Units
Temperature, T	581.4	^{o}R
Production rate, q_g	133.66	MSCF/D
Matrix permeability, k_m	3.24×10^{-5}	mD
Fracture permeability, k_f	1.0×10^{5}	mD
Gas viscosity	1.84×10^{-2}	cp
Porosity, ϕ	0.05	
Gas compressibility, c_{gi}	2.8×10^{-4}	psi^{-1}
Rock compressibility, c_r	0	psi^{-1}
Initial pressure, P_i	3,100	psi
Fracture length, L_f	164.0	ft
Fracture width, w_f	0.033	ft

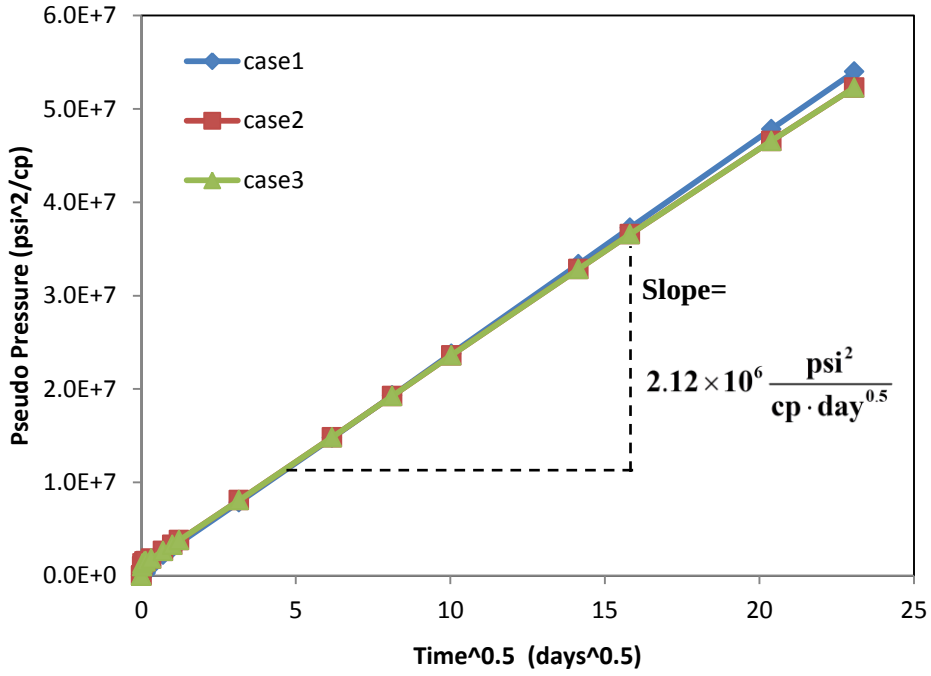

Figure 5.5 Fracture pseudo-pressure vs. square root of time for the three models

Table 5.1 lists the input parameters for simulation used in the above three fracture models. Fluid in this study is ideal methane gas which indicates that the gas Z factor always remains 1 and viscosity is a constant. Using the parameters in the table, the dimensionless hydraulic fracture conductivity is calculated as $C_{fd} = k_f w_f / k_m x_f = 7.4\times10^{6}$ and the hydraulic fracture could be treated as infinite conductivity (Cinco-Ley and Samaniego, 1981). In simulation, only one discrete grid is used to represent one stage of hydraulic fracture. Figure 5.5 shows the calculated hydraulic-fracture pseudo-pressure vs. square root of time for these three models. Calculation results all follow the straight relation between pseudo-pressure and square root of time as shown in Figure 5.5. Besides, they almost coincide with each other regardless of their fracture number and shape. This phenomenon indicates that fracture number and shape have little influence on the early transient pressure behavior for linear

flow. The linear flow equation (5.1) for single fracture can be extended to multi-stage fractures and slant fractures to estimate their fracture properties such as effective contact area.

From Equation (5.1), fracture-matrix contact area can be estimated the Equation (5.2).

$$S = \frac{200.8Tq_g}{m_{cr}\sqrt{k(\phi\mu c_t)_i}} \qquad (5.2)$$

where m_{cr} is the slope of straight line in pseudo-pressure vs. square root of time. Substitute the calculated m_{cr} and other parameters listed in Table 5.1, the calculated fracture-matrix contact area from Equation (5.2) is estimated as $1.1526\times10^4 ft^2$, while the simulation input about the fracture-matrix contact area for these three models is $1.0764\times10^4 ft^2$. Considering the gas compressibility in the numerical simulation process cannot be kept constant as shown in Figure 3.10.2, 7% error between the formulation analysis and real input data is acceptable.

This match between analytical results and numerical results give confidence on grids refinement technology used, unconventional simulator formulation and pseudo-pressure calculation.

5.1.2 Linear Flow in Natural-Fractured Formation

The previous section mainly focused on gas linear flow with hydraulic fractures in single-porosity formation. As we know, the stress alteration induced by hydraulic

fracturing may re-activate existing natural fractures, and therefore opens micro-flow channels in the drainage area of stimulated wells within the SRV. Seismic data collected in unconventional reservoirs has indicated that the stimulated areas are much larger than a simple planar fracture could create. Therefore linear flow behavior in natural-fractured formation is necessary to discuss. As the macro or micro natural fracture distribution is complex and hard to characterize in details, it is impossible to identify each natural fracture or use the discrete fracture model for simulation. Double-porosity method is adopted for this stimulated domain numerically, which is introduced in Section (3.9).

In this case, all the calculation parameters remain the same with those listed in Table 5.1. For the natural fracture properties, its porosity $\phi_{nf} = 0.0003$ and its permeability $k_{nf} = 0.324$ mD. Figure 5.1.5 shows the sketch of this model and Figure 5.1.6 presents the simulated results for hydraulic fracture grid pseudo-pressure vs. square root of time.

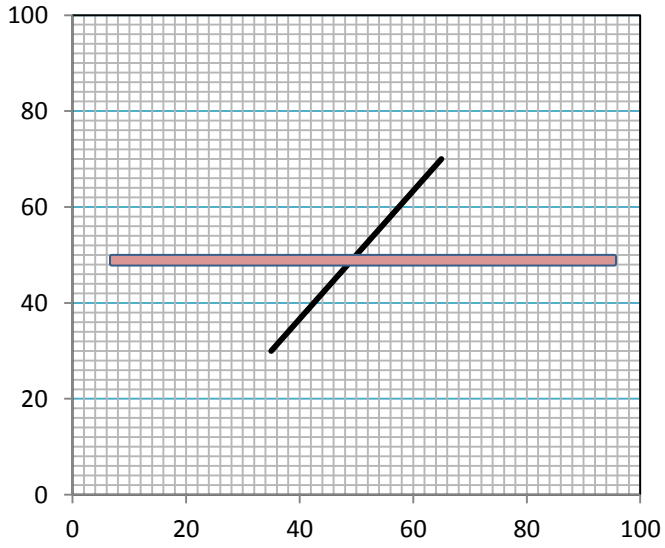

Figure 5.6 Sketch of the hydraulic fracture in natural-fractured formation

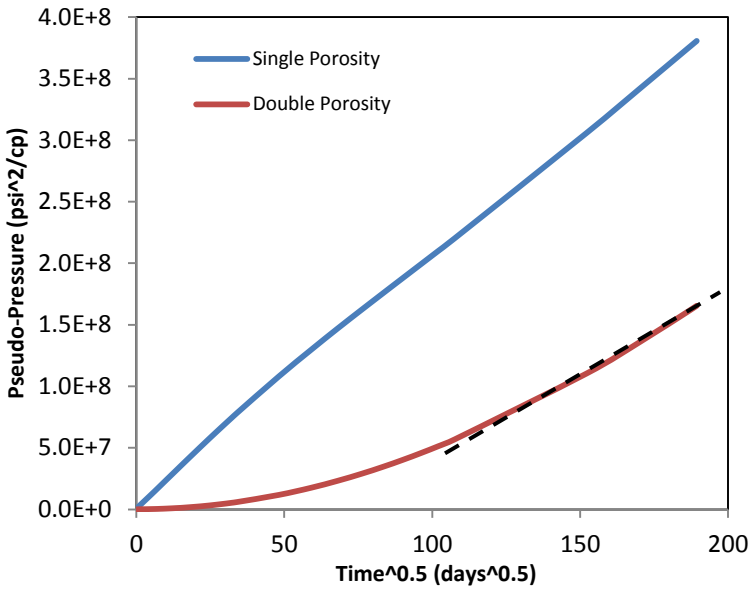

Figure 5.7 Linear flow behavior comparison for single porosity and double porosity formation during a long time

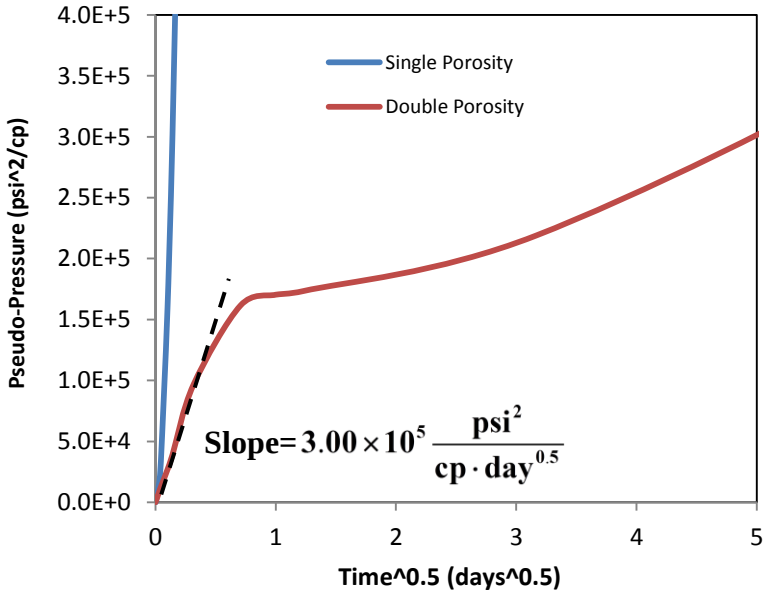

Figure 5.8 Linear flow behavior comparison for single porosity and double porosity formation during a short time

From Figure 5.7 and Figure 5.8, flow behavior in natural fractured formation does not have an obvious straight relation between pseudo-pressure and square root of time.

The slope of this curve increases with time and slow tends to a steady value. This value is a little smaller than the one from single porosity formation, providing us with an estimation of matrix properties, permeability and porosity. However, it takes long time to observe this phenomenon, about 30 years in this case. As we mentioned above, straight-line behavior is an approximation of the flow equation and it is only applicable to early time flow behavior analysis. Therefore, it is of little use for reality.

In this case, if time is zoomed in to the first 25 days, some useful information can be obtained. Pseudo-pressure builds up rapidly for the first half day in a trend of straight line. The slope of this line is $3.05\times10^{5}\,\frac{\text{psi}^2}{\text{cp}}$, as shown in the figure. Substitute this value into Equation (5.2) and replace the matrix permeability and porosity with natural fracture permeability and porosity. The calculated fracture-matrix contact area is $1.052\times10^{4}\,\text{ft}^2$, only 2% error from the input data. Thus, analysis of the early data in this case provides us an technique to estimate natural fracture properties.

5.1.3 Gas Adsorption Effect on Linear Flow

As mentioned in Section (3.10), considering adsorption effect leads to the change in accumulation term of gas flow conservation equation. The derivations in the previous sections show that this change is equivalent to adding a pressure dependent compressibility (Equation 3.33). Hence, for unconventional reservoirs in which adsorption effect cannot be neglected, only considering the compressibility derived from rock and free gas in pores could cause errors in the estimation. The flow model above (hydraulic fracture and single-porosity formation as shown in Figure 5.1.1(a)), is

modified by adding the adsorption terms to study this point. The pressure behavior comparison between the original flow model and adsorption-added flow model is shown below.

Details about the flow model with adsorption are introduced in Section (2.1.2). The Langmuir's volume V_L is supposed to be 218.57scf/ton and the Langmuir's pressure P_L is 2285.7psi. With initial reservoir pressure 3100psi and rocks average density 2.7g/cc, the initial compressibility from free gas is $2.8\times10^{-4}\text{psi}^{-1}$ and that from gas adsorption is $1.12\times10^{-4}\text{psi}^{-1}$ (Equation (3.32) and (3.33)).

Figure 5.9 shows the pseudo-pressure vs. square root of time curve with and without considering adsorption for the linear flow. The red line represents result for case with gas adsorption. It still goes in a straight line but with a different slope about $1.78\times10^{6}\ \text{psi}^2/\text{cp}\cdot\text{day}^{0.5}$, a little less than the scenario without adsorption. If this value is taken to estimate the fracture-matrix contact area by Equation (5.2) only with free gas compressibility $2.8\times10^{-4}\text{psi}^{-1}$, the calculated area is $1.373\times10^{4}\text{ft}^2$. And if the adsorption compressibility $1.12\times10^{-4}\text{psi}^{-1}$ is added to the free gas compressibility for the recalculation of the contact area, value becomes $1.157\times10^{4}\text{ft}^2$. The real input data for this area is $1.076\times10^{4}\text{ft}^2$. Figure 5.10 presents a visualized comparison between these three values.

The conclusion from this numerical test is that if Equation (5.2) is taken to estimate the fracture-matrix contact area for an unconventional reservoir, in which gas adsorption is present, not considering the adsorption effect in the equation will result in

an overestimate of the total area. One better approach is adding "adsorption compressibility" to the compressibility for calculation.

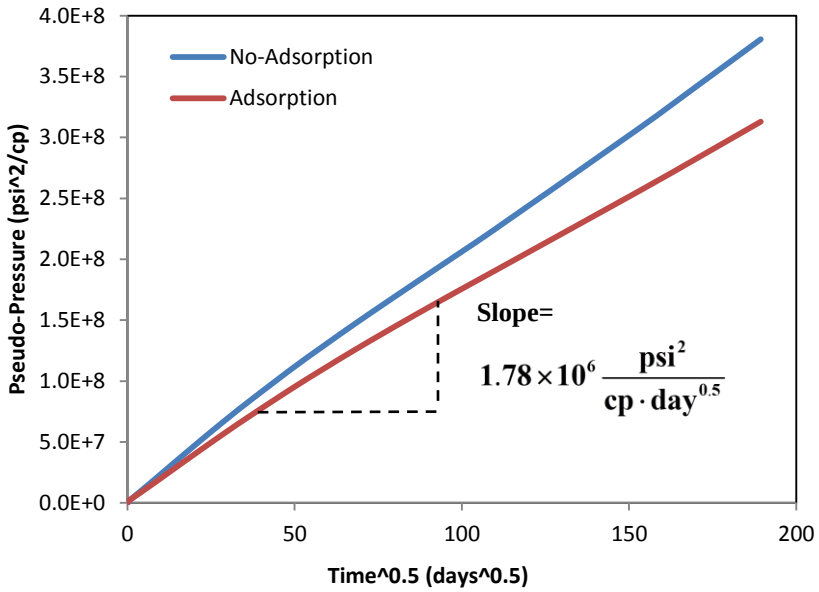

Figure 5.9 Linear flow behavior comparison between flow with and without adsorption

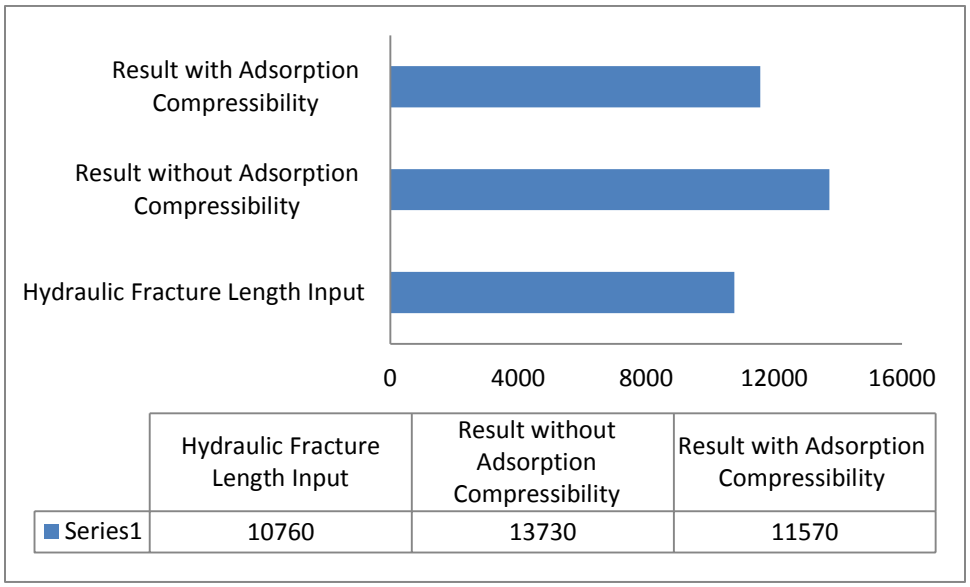

Figure 5.10 Results for analytical calculated fracture area and input data

5.2 Sensitivity Study of Non-Linear Flow Mechanisms

The following model application example is about gas flow in a horizontal well and 20-stage hydraulic fracture system in an extremely tight, uniformly porous and/or fractured reservoir (Figure 5.11). This model is designed to evaluate the influence from the above-discussed non-linear flow mechanisms on gas production. Literature review shows that there exist little detailed unconventional gas formation data, even less on the tests of unconventional phenomena, such as Klinkenberg effect and gas adsorption data. It's almost impossible to prepare the whole set of simulation input data for a specified unconventional gas field. In this example, all the data are collected separately from different papers or reports on unconventional gas study. They are critical reviewed and collected for the study below.

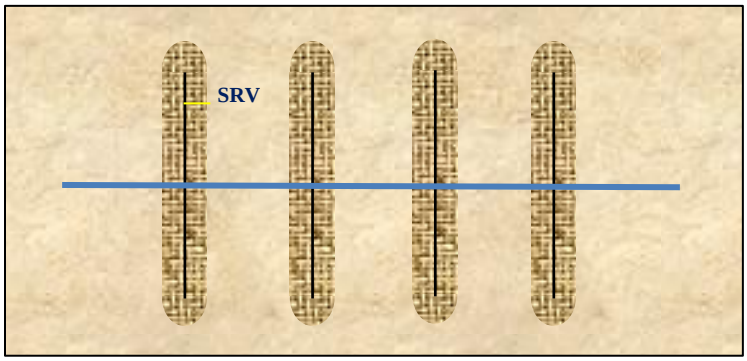

Figure 5.11 Horizontal and multi-staged hydraulic fracture model

The reservoir formation is at liquid-gas, two-phase condition. However, the liquid saturation is set at residual values as an immobile phase. Thus this is actually a single-phase gas flow problem and is modeled by the two phase flow reservoir simulator. The immobile liquid flow is controlled by liquid and gas relative permeability curves as shown below in Figure 5.12:

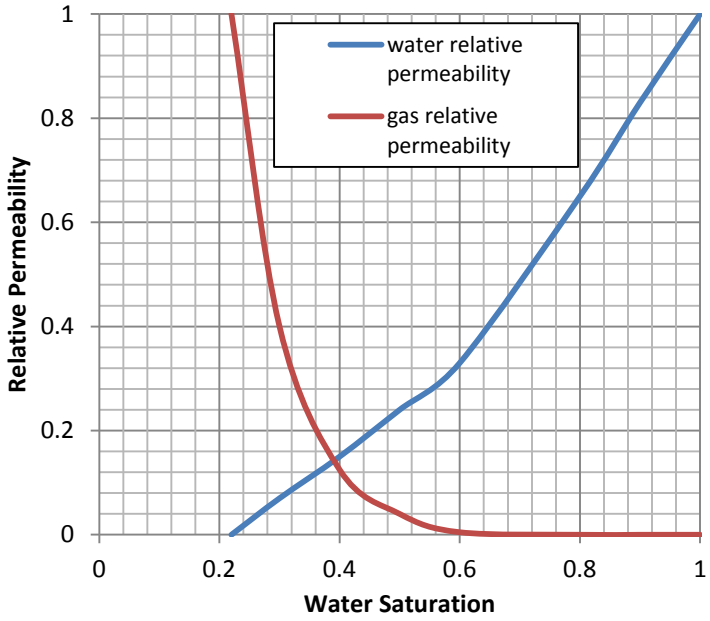

Figure 5.12 Relative permeability for gas and water phases in this calculation case

As shown in Figure 5.11, the stress alteration induced by hydraulic fracturing activated existing natural fractures, and therefore opens microfracture channels in the drainage area of the stimulated well. In this case, it is assumed that only the natural fractures within the stimulated reservoir volume (SRV) near the hydraulic fractures are active and the rest natural fractures outside the SRV remain inactive. As a result, the permeability near the well of the reservoir is significantly improved. This effect would help increase the well productivity in the initial production. To simulate the performance of this system using our model, hydraulic fractures are represented by the discrete fracture model. An active naturally-fractured reservoir area is described by the mutli-continuum fracture model, while a non-active natural fractured reservoir area is represented by the single-porosity model. Details about the hybrid-fracture model are introduced in section 3.9.

To reduce the calculation time, only one stage hydraulic fracture with its associated SRV and single porosity area (Figure 5.13) is simulated with the following two considerations. The matrix permeability is so small that flow interference between adjacent hydraulic fractures cannot be observed for a long time. Besides, we do not consider formation property variations and assume each part of this formation with the same flow pattern. Twenty times of the simulated production will be the total production for this case with horizontal wells and 20 hydraulic fractures.

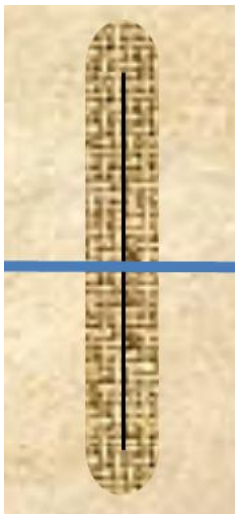

Figure 5.13 One set hydraulic fracture with its associated SRV and single porosity area

In this model, the horizontal well is only open to hydraulic fractures for flow. The well model inside the fracture plane is a 2D problem. Compared with the flow conductivity in formations, flow conductivity inside the hydraulic fracture and horizontal well can be treated as infinity. For the simulation of this example, hydraulic fracture and horizontal well are treated as a single grid. Flow between hydraulic fracture and formation is important for this problem. Due to the low permeability, it will take a long time for the system to reach semi-steady or steady state. Local grid-refinement

technology is applied near the fracture to better characterize the flow behavior near hydraulic factures, as shown in Figure 5.14.

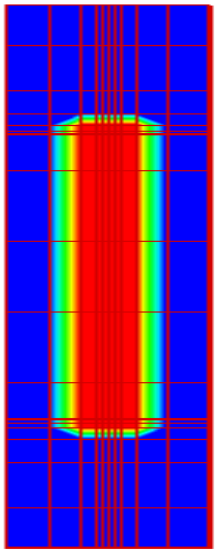

Figure 5.14 Local grid-refinements for hydraulic fractures

Fluid that flows in this reservoir is treated as real gas of methane, the Z factor and viscosity are not constant, but change with pressure. Their values are obtained online and input into the simulator in a discrete data form. Linear interpolation is done in the simulator to obtain the gas properties at specified pressure. System is assumed to be isothermal with temperature 200 ^{o}F. Z factor and viscosity curve with pressure is shown in Figure 5.15 and 5.16.

The reservoir initial pressure is 3,800psi. Gas is produced under constant wellbore pressure 1,000psi. Calculation data about Klinkenberg effect, gas adsorption and geomechanics effect are estimated from Figure 2.1, 2.3 and 2.4. All the details about the input are list in Table 5.2.

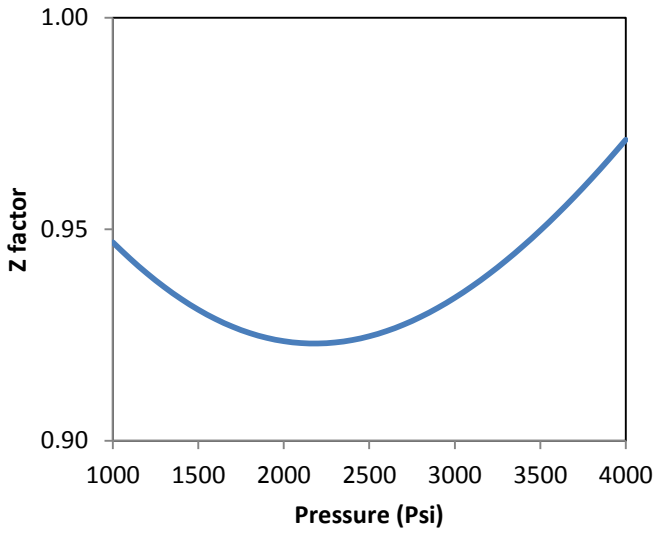

Figure 5.15 Gas Z factor with pressure in this case

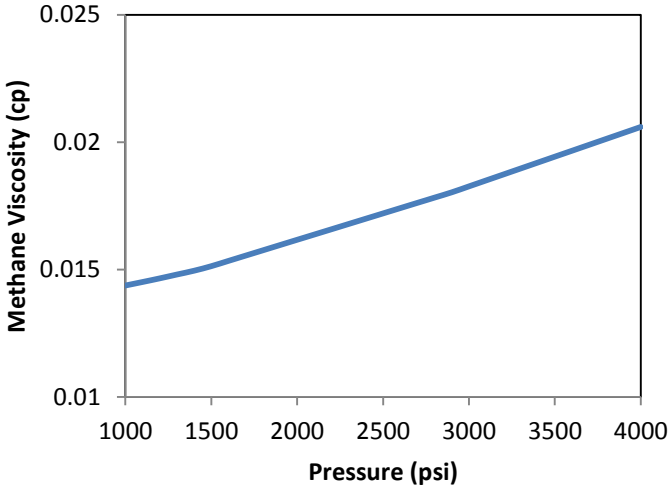

Figure 5.16 Gas viscosity with pressure in this case

Table 5.2 Data used for the second case studies

Reservoir length, Δx, ft	4000	Hydraulic fracture porosity, Φ_{hf}	0.5
Reservoir width, Δy, ft	1180	Horizontal well length, L_h, ft	3000
Formation thickness, Δz, ft	328	Initial reservoir pressure, P_i, psi	3800
Natural fracture permeability, k_{nf}, md	1.6	Natural fracture porosity, Φ_{nf}	0.001
Hydraulic fracture number	20	Reservoir temperature, T, ^oF,	200
Matrix porosity, Φ_m	0.05	Natural Fracture Spacing, m	10
Hydraulic fracture half-length, X_f, ft	590	Reservoir depth, h, ft	5800
Viscosity, μ, cp	0.0184	Langmuir's pressure, P_L, psi	2285.7
Matrix permeability, k_m, md	3.2E-05	Langmuir's volume, V_L, scf/ton	218.57
Distance between hydraulic fractures, $2y_e$, ft	200	Natural fracture total compressibility, c_{nf}, psi^{-1}	2.5E-04
Constant flowing bottomhole pressure, P_{wf}, psi	1000	Matrix total compressibility, c_{tm}, psi^{-1}	2.5E-05

5.2.1 Different Natural Fracture Distribution Analysis

Three different fracture models are studied. The first one assumes that natural fractures in the whole formation remain non-active. The second one assumes the formation has two parts, stimulated reservoir volume near the hydraulic fracture that is presented by double-porosity model and single-porosity, low-permeability area outside the SRV. The third one assumes active natural fractures in the entire formation and the formation is presented by the double-porosity model. All the other calculation parameters, such as production manner, matrix and fracture properties, hydraulic fracture width, length and height, keep the same in these three models. In addition, the non-linear phenomena of adsorption and Klinkenberg effect are not considered in this study. Figure 5.17 shows the sketches of these three models:

Figure 5.17 Three different fracture models

Figure 5.18 shows cumulative gas production with time for the above three models. Production value shown in this figure is the total amount from 20 hydraulic fractures, which is 20 times of the simulation result of the single unit. Simulation result indicates that different natural fracture distributions have apparent influence on the production. Difference between the first case and the third case is very large. For the partial and whole natural fracture distribution models, flow rate at initial is large, but declines rapidly, especially for the third model, whose production rate can be declined to near zero in about 20 years.

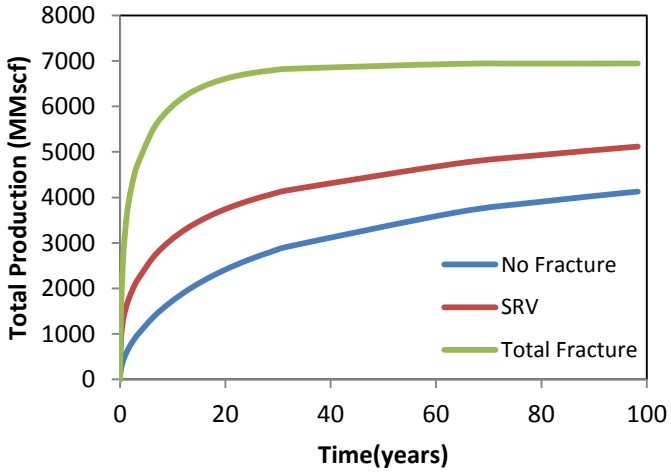

Figure 5.18 Cumulative productions with time for the three different fracture models

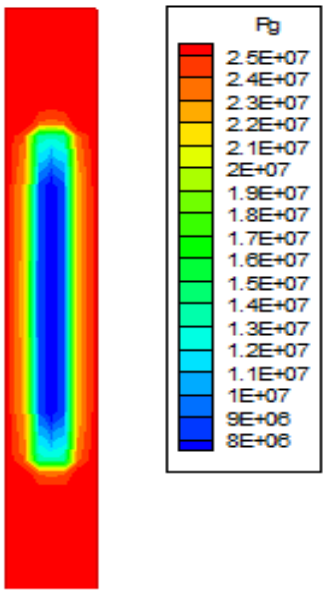

Figure 5.19 Pressure distribution at 1 year for the second fracture model (Pa)

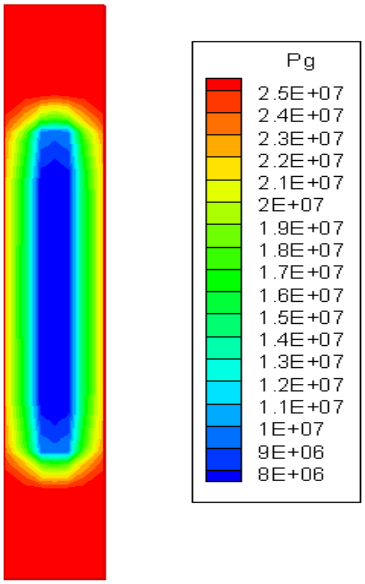

Figure 5.20 Pressure distribution at 20 years for the second fracture model (Pa)

5.2.2 Sensitivity Study of Klinkenberg Effect

Next, based on the second model (SRV), analysis is done considering the above-mentioned non-linear flow mechanisms. They are Klinkenberg, geomechanics, and gas adsorption effects. The second model is adopted because in our opinion, it is more realistic for gas production from hydraulic fractured wells in unconventional reservoirs. Effects from these non-linear flow mechanisms will be evaluated and a preliminary evaluation is given on whether they should be considered in the unconventional reservoir simulation or not.

Parameters of Klinkenberg effect are estimated using Equation (2.2) (Ozkan et al. 2010). In this equation, the correlation to compute the diffusivity constant is given by Ertekin et al. (1986):

$$D_g = \frac{31.57}{\sqrt{M_g}} k^{0.67} \tag{5.3}$$

Where D_g is in ft^2/D.

We analyze the Klinkenberg effect with three different matrix permeability, 1.0×10^{-3}md, 1.0×10^{-5}md, and 1.0×10^{-7}md, as shown in Figure 5.21 and Figure 5.22. We can see that the contribution of Klinkenberg effect is more significant at low pressures and for lower values of permeability. This estimation also provides reliable values of the b factor for analyzing Klinkenberg effect.

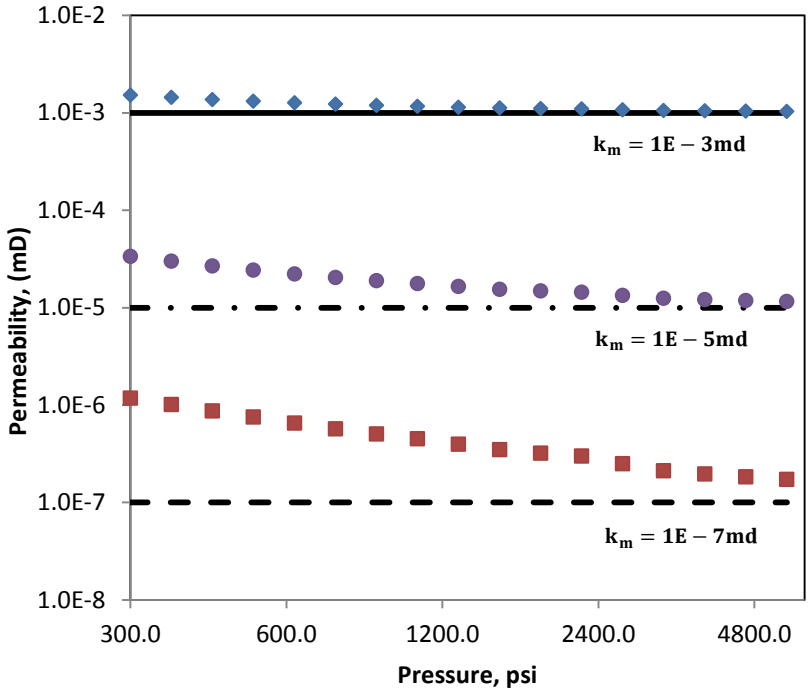

Figure 5.21 Contribution of Klinkenberg effect to the apparent matrix permeability (Ozkan et al. 2010)

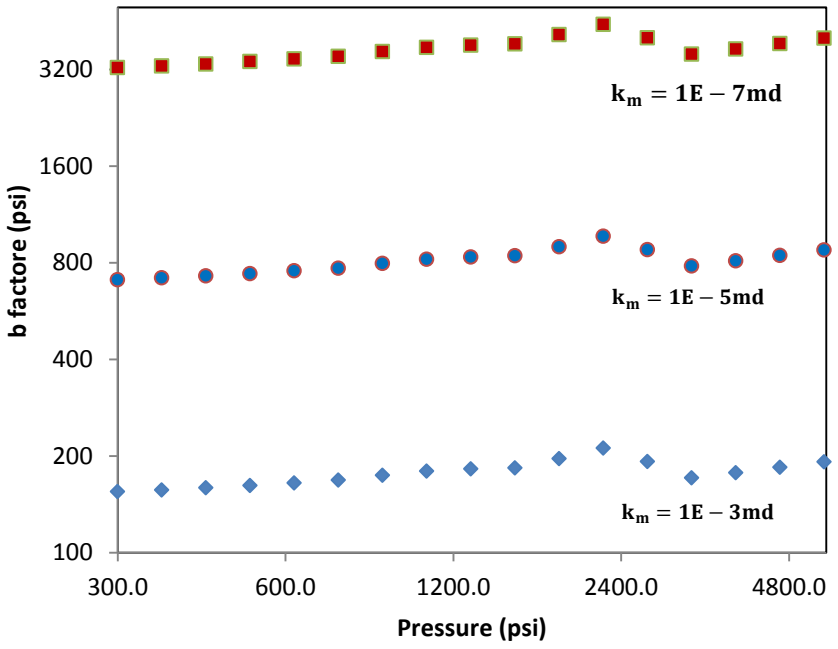

Figure 5.22 Estimations of Klinkenberg b factor for three permeability

Figure 5.23 shows the cumulative production comparison between cases with and without Klinkenberg effect. Relevant calculation parameters are obtained from Figure 5.22. Here our simulator handles the Klinkenberg b factor not as a constant value but changing with matrix permeability and pressure. As shown in Table 5.2, the input data of matrix permeability is 3.2×10^{-5}md and the initial reservoir pressure is 3800psi. With this permeability value and under higher pressure, Klinkenberg effect will not have an obvious influence on gas flow permeability based on the estimation in Figure 5.21. With the pressure of the area near wellbore and hydraulic fracture decreases quickly, Klinkenberg effect becomes important for the flow in this region. Our simulation result in Figure 5.23 also shows the influence from the Klinkenberg effect. It leads to about 10% increase to the total gas production.

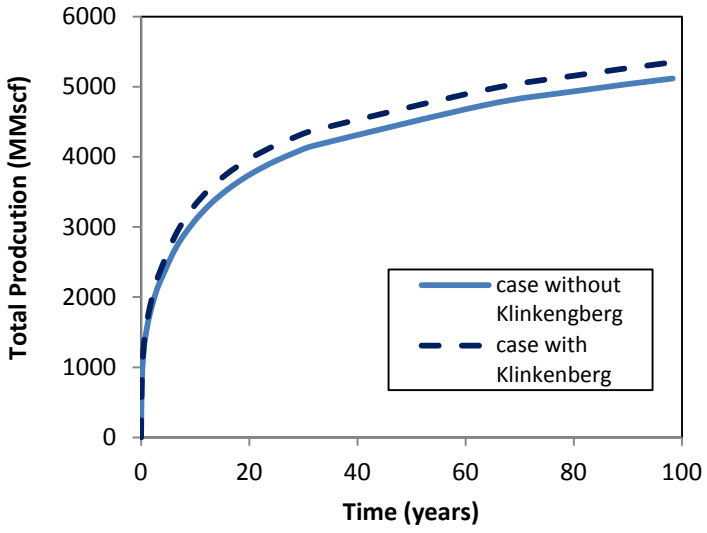

Figure 5.23 Cumulative production comparisons with and without Klinkenberg effect

5.2.3 Sensitivity Study of Geomechanics Effect

Next, geomechanics influence on the production is analyzed. Total stress is estimated to be 5,800psi according to the formation depth. The Biot constant is assumed to be 1.0 and initial pressure to be 3,800psi. Then the initial effective stress is 2,000psi. The wellbore bottom-hole pressure is 1,000psi, thus the upper limit of the effective stress range in this example is 4,800psi. We assume the change of effective stress leads mainly to the opening or closing of micro fractures. It has little influences on the matrix permeability. For this case, the above physics is considered and natural fracture porosity and permeability change with effective stress is included in the simulation. As shown in Figure 2.4, effective permeability of Barnett rock sample reduced about 50% when the effective stress increased from 2000psi to 3200psi. For the double-porosity model, the rock effective permeability can be approximately expressed as:

$$k_{eff} = k_f \phi_f + k_m \tag{5.4}$$

We mainly study the effective stress range from 2,000psi to 4,800psi in this example. Here the matrix permeability and porosity are assumed to be constant with the change of effective stress. We do not use the exact data in Figure 2.4 for effective permeability. But our input data in this example keeps the same trend with the data in Figure 2.4. The effective permeability has a semi-log linear relationship with the effective stress. Besides, we assume the linear relationship between the fracture porosity and effective stress. When the effective stress increases from 2,000psi to 4,800psi, the fracture porosity decreases from 0.001 to 0.0006. Details about the natural fracture permeability and porosity values are shown below in Table 5.3:

Table 5.3 Porosity and permeability of natural facture and matrix with effective stress

Effective Stress (psi)	ϕ_f	k_f (mD)	ϕ_m	k_m (mD)
2000	0.0010	1.600	0.05	3.20E-05
2400	0.00094	1.067	0.05	3.20E-05
2800	0.00089	0.712	0.05	3.20E-05
3200	0.00083	0.476	0.05	3.20E-05
3600	0.00077	0.318	0.05	3.20E-05
4000	0.00071	0.211	0.05	3.20E-05
4400	0.00066	0.139	0.05	3.20E-05
4800	0.00060	0.090	0.05	3.20E-05

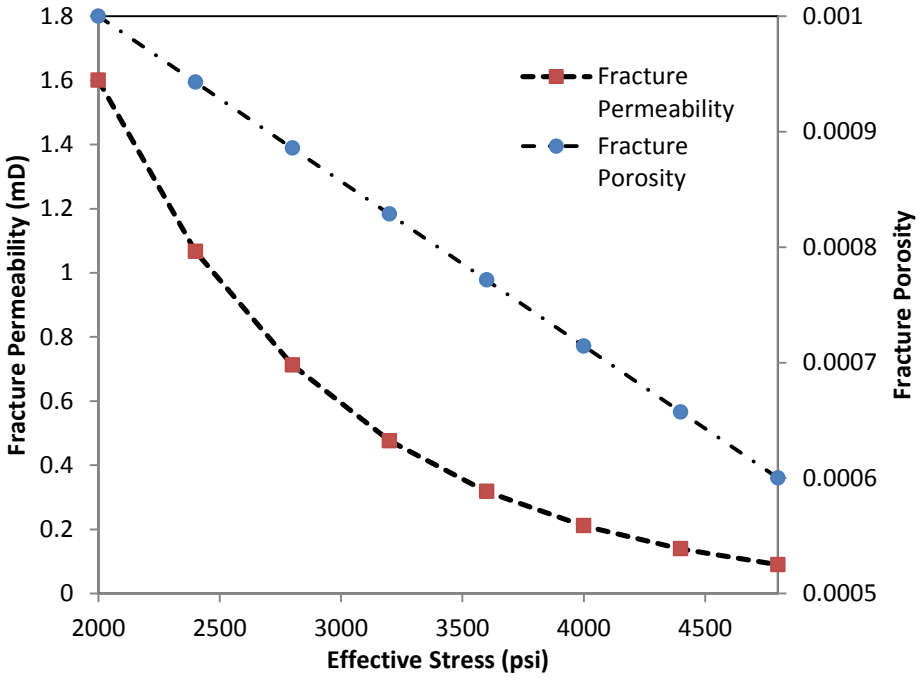

Figure 5.24 Porosity and permeability of natural facture with effective stress

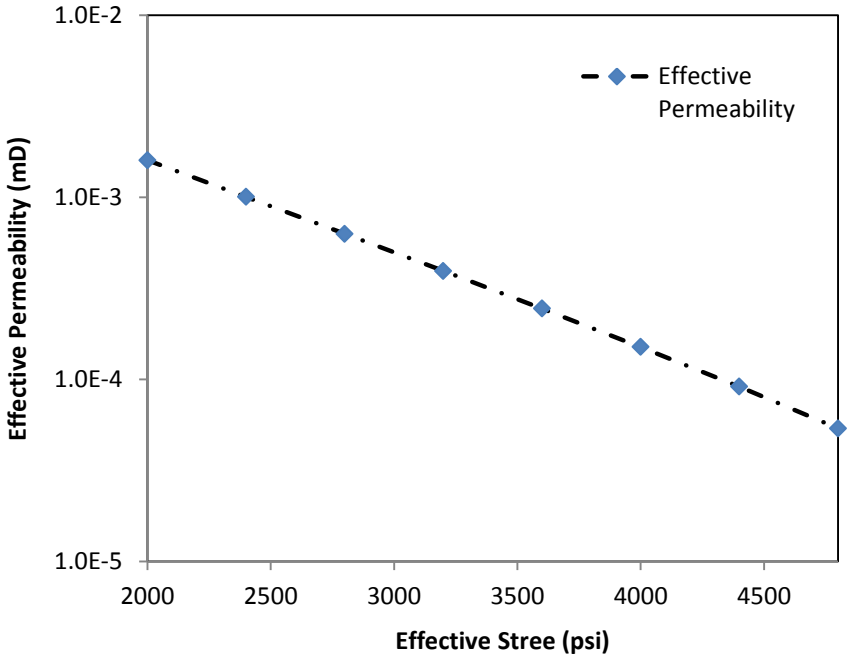

Figure 5.25 Formation effective permeability with the change of effective stress

Gas production results in the decrease in gas reservoir pressure, then the effective stress goes up. Opened natural fractures are closing consequently and gas production rate goes down. Simulation result is shown in Figure 5.26. It matches well with the above physical analysis. 10% decrease of the cumulative production for 100 years is observed in this simulation case.

5.2.4 Fully Coupling Klinkenberg Effect and Geomechanics for the Effective Permeability

Based on the above simulation result, both Klinkenberg and geomechanics effects influence the gas production apparently by changing the reservoir effective permeability. For unconventional gas reservoirs, these two non-linear flow mechanisms can exist

simultaneously. Their impacts are different. Klinkenberg effect comes from the interaction between gas molecules and pore walls. Geomechanics effect works on the micro-structure and deformation of the gas flow pores. We build an effective methodology that can fully couple these two mechanics. In one simulation iteration, the stress distribution, rocks intrinsic permeability, gas flow effective permeability and pressure distribution are calculated at the same time and they influence each other. Their connections are based on geomechanics correlations, Klinkenberg effect, fluid flow equations and geomechanics module. Figure 5.27 shows the cumulative production with time for 4 cases: 1) Flow without Klinkenberg and without geomechanics effects; 2) Flow with Klinkenberg and without geomechanics effects; 3) Flow without Klinkenberg and with geomechanics effects; 4) Flow with Klinkenberg and with geomechanics effects;

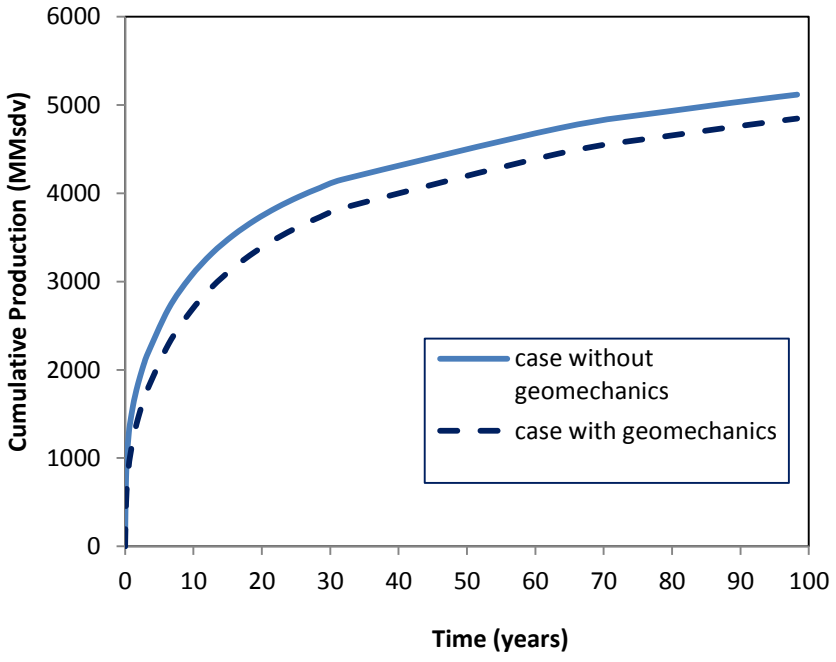

Figure 5.26 Cumulative production comparisons with and without geomechanics

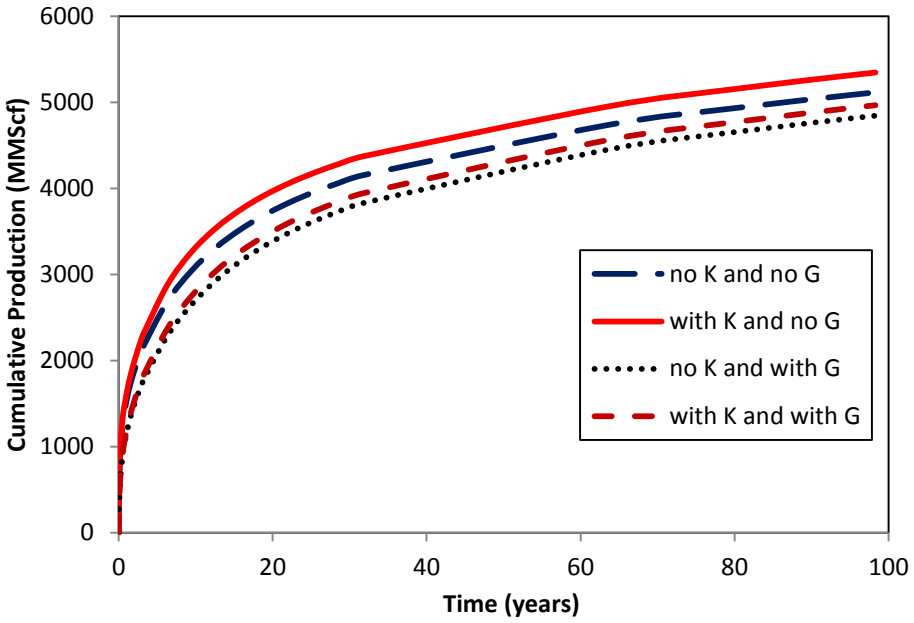

Figure 5.27 Analysis for flow coupled Klinkenberg and Geomechanics effects

5.2.5 Sensitivity Study of Gas Adsorption

Figures 5.28. 5.29 and 5.30 present results for adsorption analysis using the numerical model. Based on the data in Table 5.2, the total gas mass as free gas in micropores and adsorbed gas on rocks at initial condition is calculated, as shown in Figure 5.28. Then the cumulative gas production with and without considering adsorption is compared. Simulation results (Figure 5.2.13) show the estimated gas production will increase with considering adsorption. This difference will become more and more evident. For the situation considering gas adsorption/desorption, gas production from the adsorption is about 30% and the produced portion of the free gas consists of 70%, as shown in Figure 5.30:

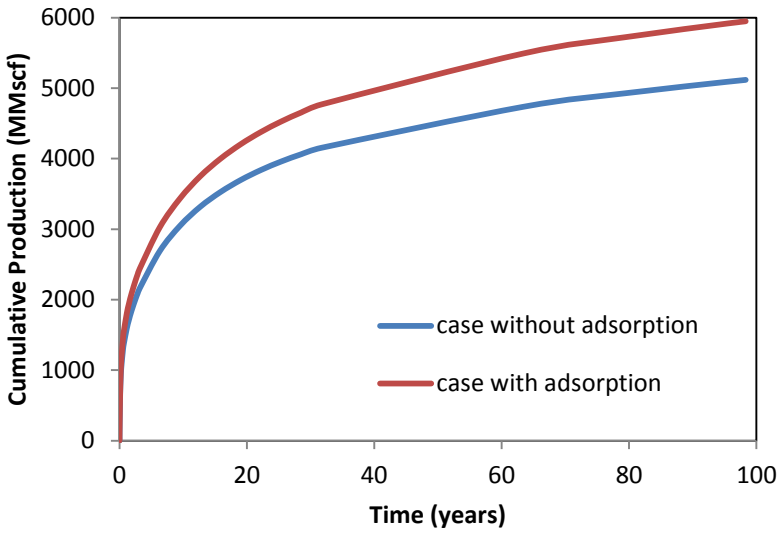

Figure 5.28 Cumulative production comparisons with and without adsorption

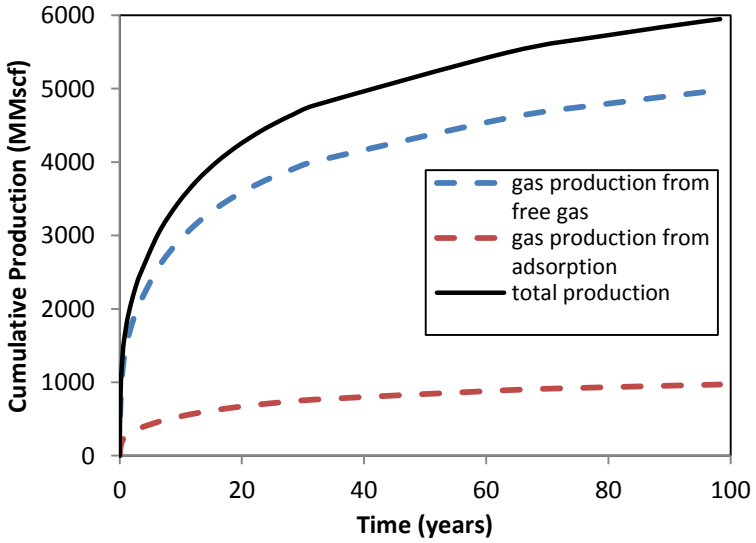

Figure 5.29 Component analyses for gas production from free gas and adsorpted gas

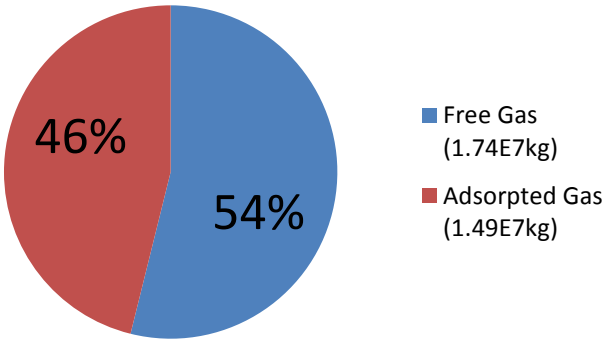

Figure 5.30 Initial gas reserve estimation from free gas and adsorbed gas

5.2.6 Sensitivity Study of Non-Darcy Flow

As we discussed above in section 2.1.3, non-Darcy flow is typically observed in high-rate gas wells when the flow in hydraulic fractures converging to the wellbore. We also mentioned that in this numerical approach, all the hydraulic fractures are merged into one grid. This is because we treat the hydraulic fracture as infinite-conductivity based on the dimensionless fracture conductivity value, C_{fd}. Cinco-Ley and Samaniego (1981) pointed out that when C_{fd} is larger than 300, flow behavior in the hydraulic fractures almost has no difference with that in an infinite-conductivity fracture. Merging all the hydraulic-fracture girds into one, however, cannot study the non-Darcy flow along hydraulic fractures, while non-Darcy flow occurs mainly during the flow inside hydraulic fractures.

First we will use our simulator to validate the conclusion from Cinco-ley and Samaniego by comparing the results from two different hydraulic fracture models. One

use multiple-grids to present the hydraulic fracture (Figure 5.31(a)) and one use single grid (Figure 5.31(b)).

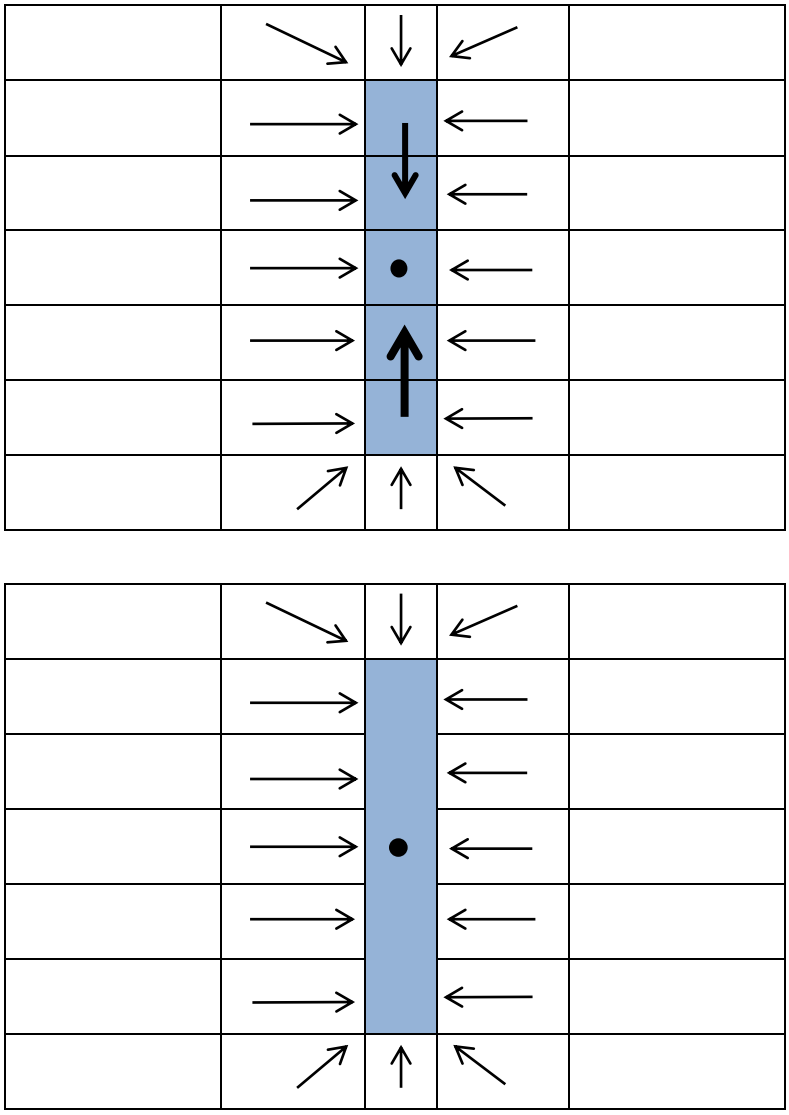

Figure 5.31 (a) Multiple-grids for the hydraulic fracture; (b) Single-grid for the hydraulic fracture

In this comparison, we assume the formation has no natural fractures and the gas is produced with constant wellbore pressure at 1,000psi. Figure 5.32 shows the simulation result. Our simulation result for this case matches well with the conclusion

from Cinco-ley and Samaniego that no difference is observed in the cumulative production with these two grid system.

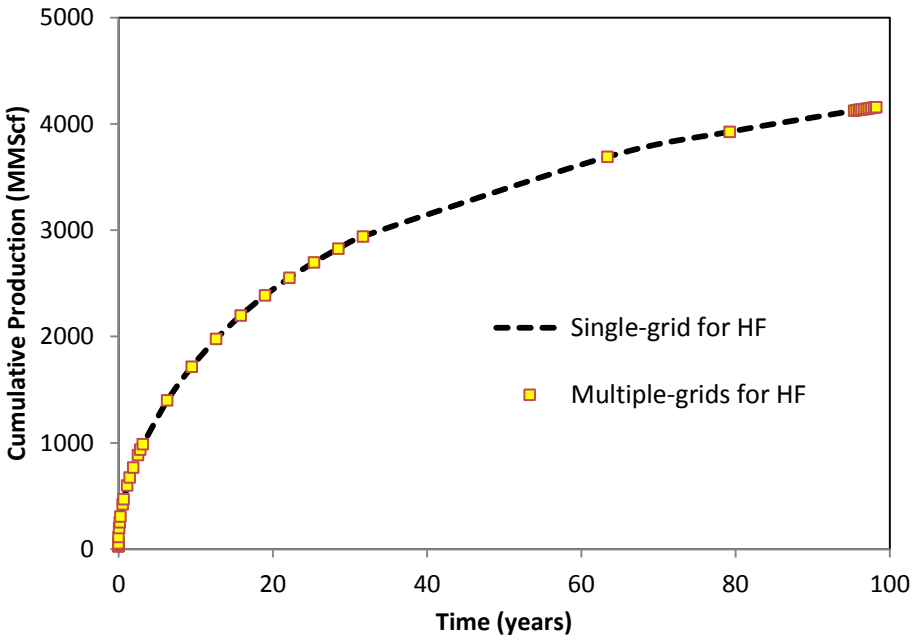

Figure 5.32 Cumulative production comparisons with single and multiple grids for HF

Based on the multi-grids hydraulic fracture model, we carry out a sensitivity study of non-Darcy flow. Because we are interested only in high-velocity domain for possible non-Darcy flow, only the hydraulic fracture blocks are activated. Rubin (2010) indicated that non-Darcy flow was not occurring within the shale itself; therefore non-Darcy flow was ignored between shale matrix grids in the analysis.

The correlation proposed by Evans and Civan is used to determine the non-Darcy flow Beta factor in the Forchheimer equation (Evans and Civan, 1994).

$$\beta = \frac{1.485 \times 10^{9}}{k^{1.021}} \tag{5.5}$$

Where the unit of k is md and unit of β is ft^{-1}. This correlation for β matched with over 180 data points including those for propped fractures (Correlation Coefficient = 0.974). In this case, the hydraulic fracture permeability is estimated as 1000md. Then the β value is $4.216\times10^{6}m^{-1}$.

With the reservoir condition parameters listed in Table 5.2, two parts in Forchheimer equation (Equation 2.4) are analyzed with different gas flow velocity, the viscosity flow term and the inertial term. Results are shown in Figures 5.33 and 5.34. We could see that fractions of the flow pressure drop for these two parts change with the gas velocity. When the flow rate is low, the inertial term is tiny compared with the viscosity flow part. Gas flow rate in the matrix or natural fractures always locate in this range so Darcy's Law is enough to characterize their flow behaviors.

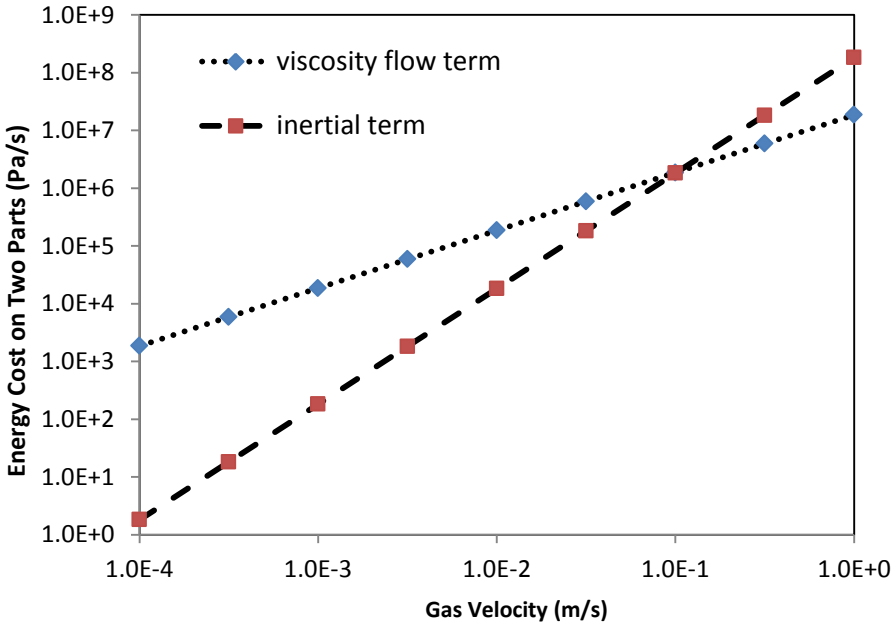

Figure 5.33 Energy cost fractions on viscosity flow term and inertial term in non-Darcy flow with gas velocity

With the increase in gas velocity, the inertial term in Forchheimer equation becomes important. This term also leads to the decrease of fracture conductivity. When the gas flow velocity is above 1.0m/s, the effective flow conductivity could be reduced by more than 90% due to non-Darcy flow. It is possible that the hydraulic fracture could not be treated as infinite-conductivity anymore based on this analysis. Figure 5.34 shows the fracture effective conductivity reductions due to non-Darcy flow.

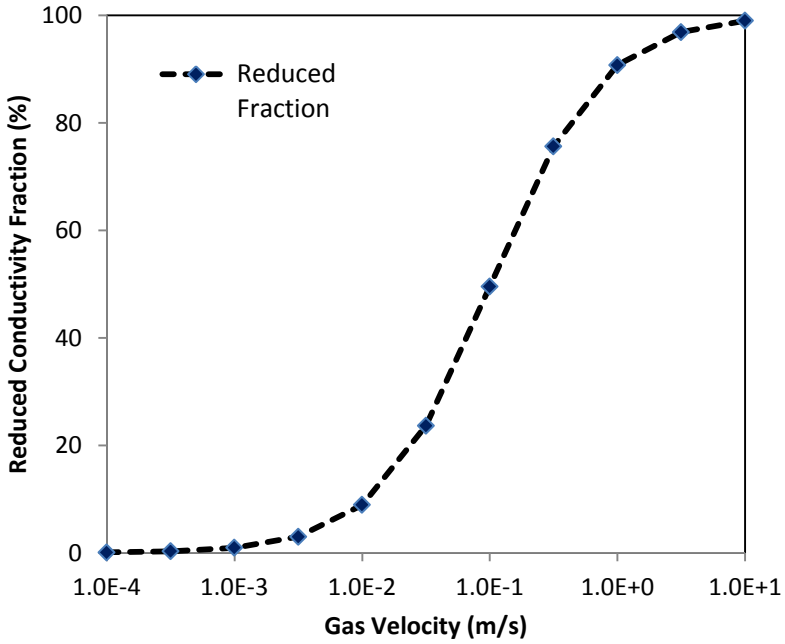

Figure 5.34 Fracture effective conductivity reductions due to non-Darcy flow

We studied the non-Darcy flow in a scenario of horizontal well plus multi-stage hydraulic fractures to see its influence on gas production. The simulation result is shown in Figure 5.35. We can see that there is no difference on the gas cumulative production between the case considering non-Darcy flow and that not considering. Non-Darcy flow does not play an important role in this case. One reasonable cause is that the original dimensionless hydraulic fracture conductivity value in this case is so large. Even with the

reduction from non-Darcy flow, its value is still large enough for the hydraulic fracture to be treated with infinite-conductivity. Therefore no difference could be observed compared the case without considering non-Darcy flow.

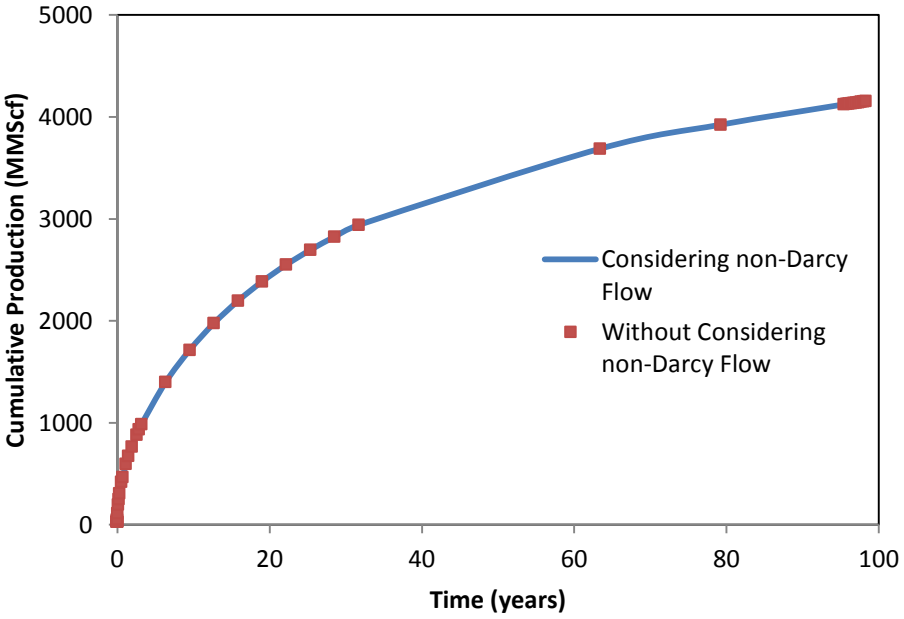

Figure 5.35 Cumulative production comparisons with and without considering non-Darcy flow

5.3 Field Example Simulation of History Matching

In this example, the unconventional gas reservoir simulator is used to study a field case. The field data for this simulation is the pressure and production rate profiles. They came from a multi-stage stimulated horizontal well in Barnett shale play. This field data is provided by Dr. Ozkan for this case study. Figure 5.36 shows the pressure and production rate data for three years.

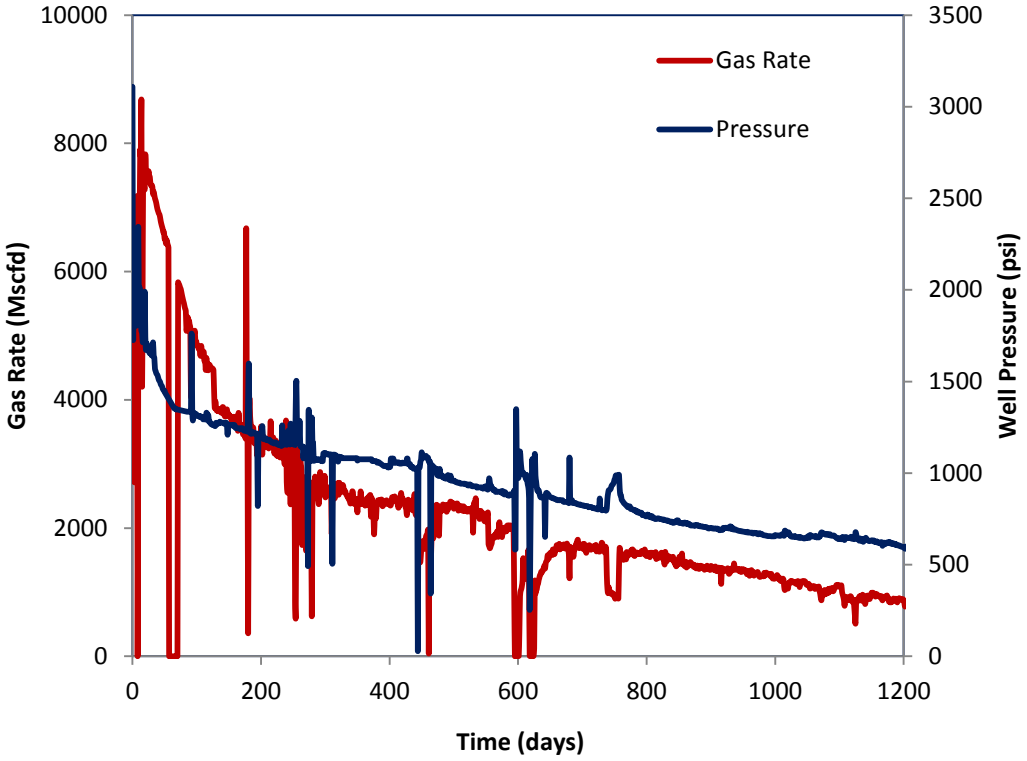

Figure 5.36 Daily pressure and production rate profiles from the field data

Table 5.4 Raw data from the company

Initial pressure, p_i, psia	3,109
Formation thickness, ft	300
Formation temperature, T, °F	106
Well radius, r_w, ft	0.23
Number of hydraulic fractures	19
Horizontal well length,L,ft	3,250
Matrix porosity, Φ_m	0.04
Fracture half-length, X_f, ft	275
Specific gravity, γ	0.588
Gas saturation, S_g	0.9
Water saturation, S_w	0.1

Apart from the pressure and production rate data, the gas company also measures and provides some useful information about this reservoir such as the initial pressure, average porosity, gas saturation and so on. They are shown in Table 5.4. However, these data are not enough for the simulation and some other important parameters need to be estimated. Without the support of enough field data experiment, gas adsorption, Klinkenberg effect and geomechanics effect are not considered in this case.

Brown and Ozkan analyzed the same data and they plotted the rate-modified pseudo pressure responses as a function of the square root of time, as shown in Figure 5.27. It shows that "hydraulic fracture and matrix" linear flow takes the main part in the early time because linear relation is observed between the above two. Its slope is $7733\frac{\text{psi}^2\text{d}^{1/2}}{\text{cp}\cdot\text{Mscf}}$.

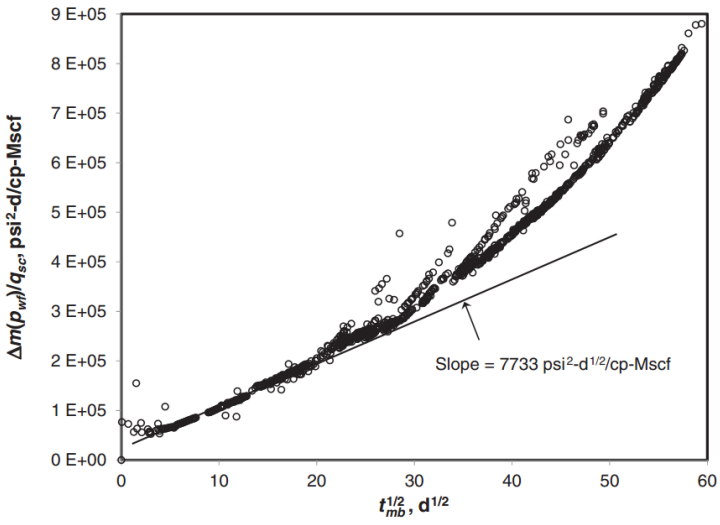

Figure 5.37 Linear-flow analysis of the field data

All the hydraulic fractures are assumed to fully penetrate the studied formation in the vertical direction and SRV is the area within 30 meters of the hydraulic fractures. Similar with the last case, only one set hydraulic fracture and its surrounding area are simulated. Refined grid and the sketch show of this area are shown below:

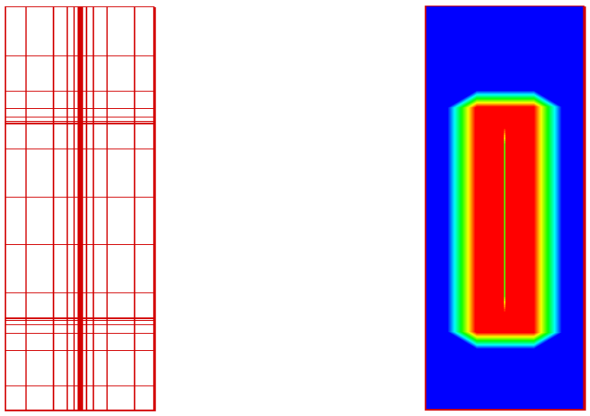

Figure 5.38 Refined grids for the field case study and model sketch

As shown in Figure 5.38, the red part is stimulated reservoir volume and the blue part is the area with lower flow permeability. The concept of effective continumm model (Wu, 1998) is adopted here so that SRV area is treated as one continumm that combines the matrix and natural fractures. With some adjustment to match the history data, the final equivilient permeability of the SRV area is set as $2.5\times10^{-4}\text{mD}$ and the blue part is $3.2\times10^{-5}\text{mD}$.

The curve of wellbore pressure with time in the first 240 days is input as a calculation data, as shown in Figure 5.39. With the well-built model, calculated production rate is compared with the real data. They matched very well to each other and thus our simulation model about the unconventional gas reservoir can be applied to the real data analysis and economy forecast (Figure 5.40).

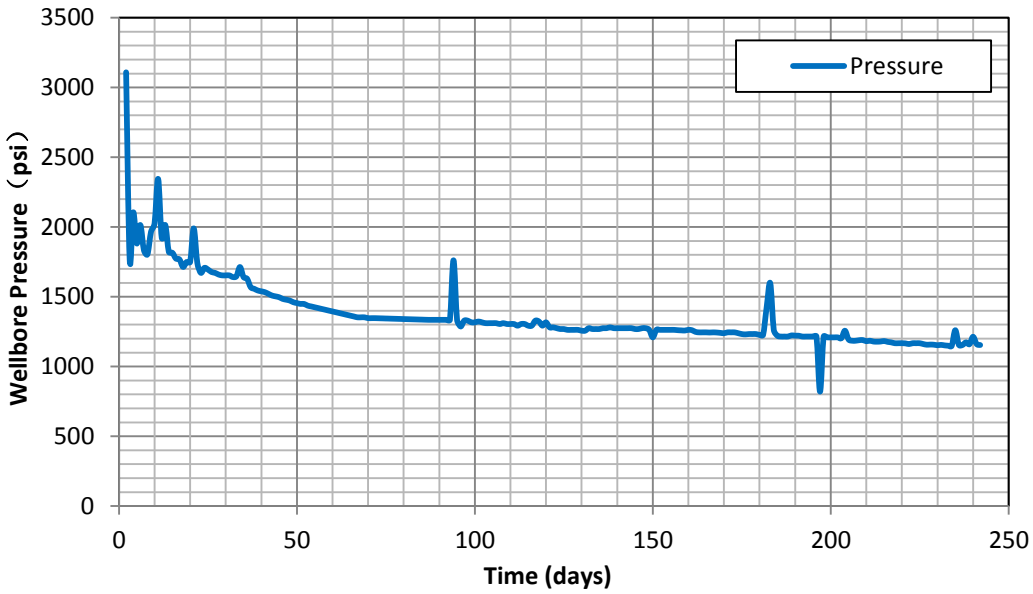

Figure 5.39 Wellbore pressure data in the first 240 days for calculation

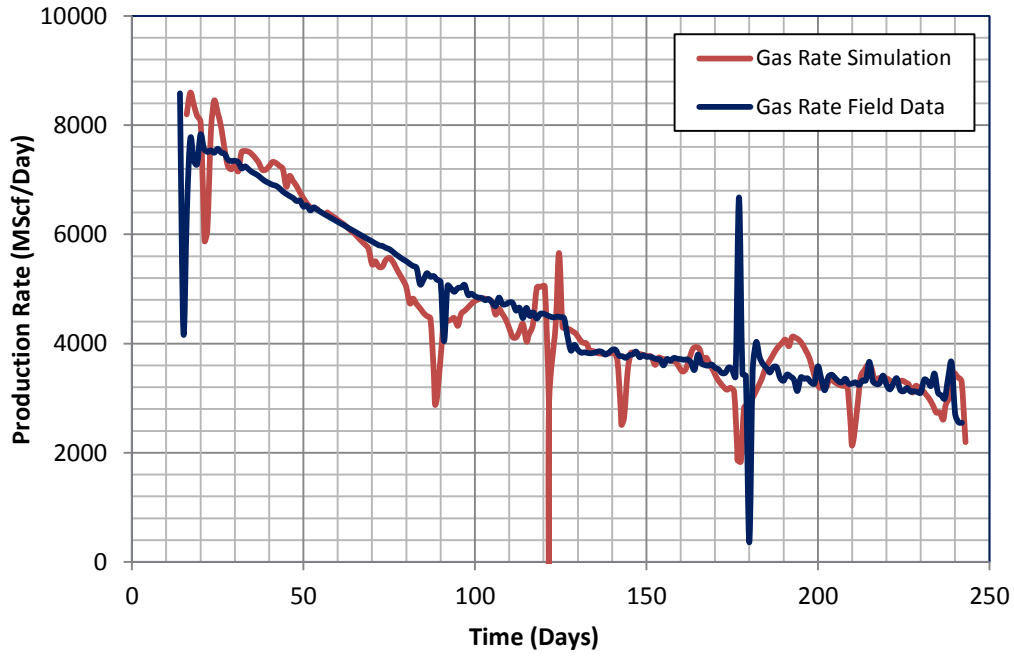

Figure 5.40 Calculated and field recorded production rate comparision

CHAPTER 6

CONCLUSIONS AND FUTURE WORK

This thesis explores the simulation of unconventional gas reservoir. It provides comprehensive discussion as well as modeling approaches of several non-linear flow mechanisms, such as Klinkenberg effect, non-Darcy flow, gas adsorption/desorption and geomechanics effect. In particular, this work demonstrates how to couple these mechanisms into a general reservoir simulator, and provides recommendations on whether they should be considered in the field reservoir simulation. In addition, a hybrid fracture model is proposed and used in this thesis to simulate the complex system of fractured horizontal wells in unconventional reservoirs. Discrete fracture model is adopted to simulate the hydraulic fractures, dual-continuum or MINC model for natural-fractured SRV surrounding hydraulic-fractures, and single porosity model for the area outside SRV.

6.1 Conclusions

1. We discussed a generalized framework mathematical model for modeling gas production from unconventional gas reservoirs. The model formulation incorporates known nonlinear flow processes, associated with gas production from low-permeability unconventional reservoirs, including Klinkenberg, non-Darcy flow, and nonlinear adsorption effects. The model formulation and numerical scheme are based on a generalized two-phase gas and liquid flow model using unstructured grids.

2. Klinkenberg effect is discussed through theoretical and experimental views. It is coupled in the simulator with model results verified by comparing with analytical solutions. Based on limited field experiment data, we evaluate its influence on gas flow based on the numerical tests. The result shows Klinkenberg effect is significant for the low-pressure reservoirs. For deep shale gas plays, the extremely low permeability makes Klinkenberg effect as apparent as that in low pressure-pressure reservoirs. However, Klinkenberg effect is expected to be strong in shales near flowing fractures as the pressure is lowered enough.

3. Non-Darcy flow effect is studied. Theoretical analysis shows that it will only be significant when the flow rate is very high. For unconventional gas reservoirs, it mainly occurs inside the hydraulic fractures especially flow converges to the horizontal well. For most cases, flow-conductivity capacity in hydraulic fracture is much larger than that in matrix, which means that the fracture conductivity is so huge that flow in hydraulic fractures can be treated with infinity conductivity. For this work, one grid is enough for representing the whole hydraulic fractures. Thus, non-Darcy flow cannot be modeled for flow inside hydraulic fractures in the approach of single grid for hydraulic fracture. We also build an approach using multi-grids for hydraulic fracture to study the non-Darcy flow. Based on our data for fractures and non-Darcy flow parameters, little difference is observed between simulation results for cases with and without considering non-Darcy flow.

4. Gas adsorption/desorption is incorporated into the simulator and the results are verified. Langmuir's isotherm model is mainly used in this thesis. Based on the gas adsorption data from EIA, we estimate the Langmuir pressure and Langmuir

volume for the calculation. Our simulation results show that it could contributes about third of the total gas reserves and production. For pressure transient analysis, an alternative and easy way to handle gas adsorption is the introduction of an additional “adsorption compressibility factor”. Neglecting adsorption could leads to wrong estimation of hydraulic fracture length and gas production.

5. A simplified geomechanics and flow coupling model is done in this thesis, which only considers the change of permeability and porosity due to the change of effective stress with constant total stress. In this approach, mean stress correlation is adopted. We also analyzed geomechanics influence based on the published field data. Geomechanics effect could have significant impact on gas flow when the micro-fractures close or re-open.

6. We proposed a hybrid-fracture conceptual model to characterize the complex fracture system in unconventional reservoirs. Discrete fracture model is adopted to simulate the hydraulic fractures. We use dual-continuum model to simulate the near-hydraulic-fracture, natural-fractured SRV area and use single porosity model to represent the area outside SRV. An effective methodology of gridding and simulation is built for this hybrid-fracture model to run in our simulator including the pre-process and post-process parts.

7. Grid refinement technology is introduced to accurately simulate irregular hydraulic fractures. This approach is verified by comparing with the “fracture-matrix” linear flow analytical solutions.

8. Modeling study based on this grid refinement technology indicates that hydraulic fracture total contact area with matrix is the main parameter that influences early flow behavior regardless of the hydraulic fracture number and shapes. Combined with the analytical results, the total fracture-matrix contact area can be estimated.

9. A field application example with history data matching is carried out in this study. With the input of daily pressure profile and relevant adjusted formation information, the calculated production rate matched pretty well with the field-recorded production rate data. It indicates this simulator is able to handle field simulations. This matched simulation result also helps us to better understand in this shale plays that "fracture-matrix" linear flow is a critical role in production and there does exist a SRV around the hydraulic fractures.

6.2 Future Works

1. We will keep tracking the latest study on the shale gas reservoir characterizations and simulation and continue improving the simulator according to the latest study. We also hope to collaborate with academy organizations or industry to collect more field data for model application. A full set of the field data including parameters of the Klinkenberg effect, gas adsorption, non-Darcy flow and geomechanics effect will help for better understanding and modeling of flow behavior in unconventional reservoirs.

2. Geomechanics module in this simulator is only a simplified version. A fully coupled model between geomechanics and fluid flow will be developed.

NOMENCLATURE

Symbol	Description (unit)
A_{ij}	area between connected grid blocks i and j (m^2).
b	Klinkenberg effect factor (Pa)
B_β	formation volume factor for phase β;
B_w^o	formation volume factor of water at initial bubble point pressure, P_b^o.
C_r	rock compressibility (1/Pa).
d	diameter of wellbore (m).
C_β	compressibility of liquid phase β (β = w or o) (1/Pa).
D, D_i	depth of a grid block center (m).
d1, d2	distance from center of first and second element, respectively, to their common interface (m).
d_1, d_2	distance from center of first and second element, respectively, to their common interface (m).
g	magnitude of gravitational acceleration (m/s^2).
G	minimum pressure gradient for a Bingham fluid flow (Pa/m).
H	consistence constant of a power-law fluid ($Pa.s^n$)
k	porous medium permeability (m^2).
$k_{r\beta}$	relative permeability to phase β (β = w or g).
m	time step level for the AIM scheme (=n for IMPES nodes and =n+1 for fully implicit nodes).
M	molecular weight of air.
n	previous time step level; also used to denote exponential index of a power law fluid.

N total number of grid blocks of a grid.

P pressure (Pa).

P^o reference pressure (Pa).

P_{cgw}^{gw} gas-water capillary pressure in a gas-water, two-phase system (Pa).

P_w wellbore or water phase pressure (Pa).

P_β pressure in phase β (β = w, o, or g) (Pa).

q mass rate (kg/s) or volumetric rate (m^3/s) of a phase in a source element.

q_β mass rate of generation of phase β in a source element ($kg/s/m^3$).

Q_β mass rate of generation of component β (β= w, o, or g) in a source element (kg/s).

$Q_{\beta,w}$ mass rate of component β (β= w, o, or g) in a well element (kg/s).

R universal gas constant (mJ/mole K).

r_e effective grid block radius (m).

R_i^β residual term of mass balance of component β (β= w, o, or g) at element i.

R_s solution gas-oil ratio (m^3/m^3).

r_w well radius (m).

s well skin factor, dimensionless.

S_β saturation of phase β.

$S_{\beta r}$ residual saturation of phase β.

$\bar{S}_g$ normalized gas saturation.

$\bar{S}_L$ normalized liquid saturation.

$\bar{S}_w$ normalized water saturation.

t time (seconds).

Δt time step (seconds).

T formation temperature (℃).

T^0 reference formation temperature (℃).

V_i volume of element i (m^3).

$\vec{V}_\beta$ Darcy's velocity of phase β (m/s).

v_{dg} volume of dissolved gas (m^3).

v_β volume of phase β (m^3).

$(v_\beta)_{RC}$ volume of a given mass of phase β at reservoir conditions (m^3).

$(v_\beta)_{STC}$ volume occupied by the same mass of phase β at standard conditions (m^3).

x,y,z three Cartesian coordinates with z being in the vertical direction (m).

Z gas Z factor to collaborate real gas density from ideal gas density

Creek Symbols

α_{go} biot factor for effective stress correlation

ϕ effective porosity of formation.

ϕ^o effective porosity of formation at reference conditions.

γ_{ij} transmissivity between node i and j (m^3).

$\nabla\Phi$ potential gradient (Pa/m).

$\nabla\Phi_e$ effective potential gradient of a Bingham fluid.

$\nabla\Phi_\beta$ potential gradient of phase β , (Pa/m).

η_i a set of neighboring nodes of node i.

λ_β mobility of phase β.

μ_{nn} viscosity of a non-Newtonian fluid (Pa•s).

μ_β viscosity of phase β (Pa•s).

ρ density (kg/m^3).

ρ_β density of phase β at reservoir conditions (kg/m^3).

ρ_R density of rock grains (kg/m^3).

$(\rho_\beta)_{STC}$ density of phase β at standard condition (or storage tank conditions) (kg/m^3).

σ_{gw} interfacial tension between gas and water (Pa/m).

Subscript

a air.

e effective.

f fracture or fluid.

g gas.

i index of grid block i or initial.

j index of grid block j.

ij between two connected grid blocks i and j.

ij+½ appropriate averaging between two grid blocks i and j.

ir irreducible.

k primary variable index.

L liquid.

m matrix or mass.

max maximum.

min minimum.

n NAPL.

o oil.

p Newton iteration level.

r	residual, relative, or rock.
rne	relative to a Newtonian fluid.
rnn	relative to a non-Newtonian fluid.
w	water or well.
x	x-direction.
β	phase β.

Superscript

n	previous time step level.
n+1	current time step level.
o	reference condition.
w	well.
x	x-coordinate.
β	phase β.

REFERENCES CITED

Al-Hussainy R., H.J. Ramey Jr., and P.B. Crawford, 1966, "The Flow of Real Gases Through Porous Media", Journal of Petroleum Technology, Volume 18, Number 5, May.

Barry Rubin, 2010, "Accurate Simulation of Non-Darcy Flow in Stimulated Fractured Shale Reservoirs", SPE 132093, presented at the 2010 SPE Western Regional Meeting held in Anaheim, California, USA

Blasingame, T.A., 2008, "The Characteristic Flow Behavior of Low-Permeability Reservoir Systems," SPE 114168, presented at the 2008 SPE Unconventional Reservoirs Conference held in Keystone, Colorado, U.S.A., 10–12 February.

Brown, M., E. Ozkan, R. Raghavan and H. Kazemi, 2009, "Practical Solutions for Pressure Transient Responses of Fractured Horizontal Wells in Unconventional Reservoirs", SPE 125043, presented at SPE Annual Technical Conference and Exhibition, 4-7 October, New Orleans, Louisiana

Brunauer, S., P. H. Emmett and E. Teller, 1938, J. Am. Chem. Soc.,60, 309. doi:10.1021/ja01269a023

Bustin, R.M., A.M.M. Bustin, X. Cui, D.J K Ross, and V.S. Murthy Pathi, 2008, "Impact of Shale Properties on Pore Structure and Storage Characteristics," SPE 119892, presented at the SPE Gas Production Conference, 16-18 November, Fort Worth, Texas.

Cinco-Ley, H., and Samaniego-V., F., 1981, "Transient Pressure Analysis for Fractured Wells", Journal of Petroleum Technology, Vol. 33, Num. 9.

Cipolla, C.L., E.P. Lolon, J.C. Erdle, and B. Rubin, 2010, "Reservoir Modeling in Shale-Gas Reservoirs," Reservoir Evaluation & Engineering, August.

Cipolla, C.L., N.R. Warpinski, M.J. Mayerhofer, E.P. Lolon, and M.C. Vincent, 2009, "The Relationship Between Fracture Complexity, Reservoir Properties, and Fracture Treatment Design," SPE 115769 presented at the SPE ATC&E, Denver, Colorado, U.S.A.

Cipolla, C.L., 2009, "Modeling Production and Evaluating Fracture Performance in Unconventional Gas Reservoirs," JPT, Distinguished Author Series, pp.84-90, September.

EIA (U.S. Energy Information Administration), 2011, “Review of Emerging Resources: U.S. Shale Gas and Shale Oil Plays”, July.

Erdal Ozkan, R. Raghavan and O.G. Apaydin, 2010, “Modeling of Fluid Transfer from Shale Matrix to Fracture Network”, SPE 134830 presented at the SPE ATC&E, Florence, Italy

Ergun, S., 1952, “Fluid Flow through Packed Columns”, Chemical Engineering Progress, Vol. 48, No 2. 89-94.

Ertekin, T., G.R. King and F.C. Schwerer, 1986, “Dynamic Gas Slippage: A Unique Dual-Mechanism Approach to the Flow of Gas in Tight Formations”, SPE Formation Evaluation. Vol. 1, Num. 1.

Evans, R.D., and Civan, F., 1994, “Characterization of Non-Darcy Multiphase Flow in Petroleum Bearing Formation”, Final Report for U.S. Department of Energy Assistant Secretary for Fossil Energy

Forchheimer, P., 1901, “Wasserbewgung durch Boden”, Zeitschirift des Vereines Deutscher Ingenieuer, 45 edition.

Freeman, C.M., G.J. Moridis, D. Ilk, D. and T.A. Blasingame, 2010, “A Numerical Study of Transport and Storage Effects for Tight Gas and Shale Gas Reservoir Systems,” SPE 131583, presented at the SPE International Oil & Gas Conference and Exhibition held in Beijing, China, 8-10 June.

Freeman, C.M., G.J. Moridis, and T.A. Blasingame, 2009a, “A Numerical Study of Microscale Flow Behavior in Tight Gas and Shale Gas Reservoir Systems,” Proceedings, 2010 TOUGH Symposium, Berkeley, CA, 14-16 September.

Freeman, C.M., G.J. Moridis, D. Ilk, , and T.A. Blasingame, 2009b, “A Numerical Study of Tight Gas And Shale Gas Reservoir Systems,” SPE 124961, presented at the SPE Annual Technical Conference and Exhibition, New Orleans, Louisiana, 4-9 October.

Karimi-Fard, M., L.J. Durlofsky and K. Aziz, 2004, “An Efficient Discrete-Fracture Model Applicable for General-Purpose Reservoir Simulators”, SPE Journal, Vol. 9, Num. 2.

Kelkar M. and M. Atiq, 2010, “Upgrading Method for Tight Gas Reservoirs,” SPE 133301, presented at the SPE Annual Technical Conference and Exhibition, Florence, Italy, 19-22 September.

Klinkenberg, L.J., 1941, "The Permeability of Porous Media to Liquids and Gases," in API Drilling and Production Practice, 200–213.

Kundt, A., and Warburg, E, 1875, "Uber Reibung and Warmeletitung verdunnter Gase (On friction and heat conduction of diluted gases)", Annalen der Physik Vol. 155,337.

Langmuir, I., 1916 "The constitution and fundamental properties of solids and liquids," Journal of the American Chemical Society, 38 (11): 2221–2295.

Lee, A.L., M.H. Gonzalez and B.E. Eakin, 1966, "The Viscosity of Natural Gases", Journal of Petroleum Technology, Vol. 18, Num. 18.

Mengal, S.A. and R.A. Wattenbarger, 2011, "Accounting For Adsorbed Gas in Shale Gas Reservoirs," SPE 141085, presented at the SPE Middle East Oil and Gas Show and Conference held in Manama, Bahrain, 25–28 September.

Moridis, G.J., T.A. Blasingame and C.M. Freeman, 2010, "Analysis of Mechanisms of Flow in Fractured Tight-Gas and Shale-Gas Reservoirs", SPE 139250, presented at SPE Latin American and Caribbean Petroleum Engineering Conference, 1-3 December, Lima, Peru.

NIST, National Institute of Standards and Technology, Material measurement laboratory, http://webbook.nist.gov/cgi/cbook.cgi?ID=74-82-8.

Nobakht, M. and C.R. Clarkson, 2012, "A New Analytical Method for Analyzing Linear Flow in Tight/Shale Gas Reservoirs: Constant-Rate Boundary Condition", *SPE Reservoir Evaluation & Engineering*, Volume 15, Number 1, February.

Peng, D. Y., and Robinson, D. B., 1976. "A New Two-Constant Equation of State". Industrial and Engineering Chemistry: Fundamentals 15: 59–64. doi:10.1021/i160057a011.

Pruess, K. and T.N. Narasimhan, 1985. "A practical method for modeling fluid and heat flow in fractured porous media", Soc. Pet. Eng. J., 25(1), 14-16.

Pruess, K., C. Oldenburg and G. Moridis, 1999, "TOUGH2 User's Guide", Version 2.0, Report LBNL-43134, Berkeley, California: Lawrence Berkeley National Laboratory.

Pruess, K., 1983, “GMINC-A mesh generator for flow simulations in fractured reservoirs”, Report LBL-15227, Berkeley, California: Lawrence Berkeley National Laboratory.

Rubin, B., 2010, “Accurate Simulation of Non-Darcy Flow in Stimulated Fractured Shale Reservoirs,” SPE 132093, presented at the SPE Western Regional Meeting held in Anaheim, California, USA, 27–29 May.

Silin, D. and T. Kneafsey, 2011, “Gas Shale: From Nanometer-scale Observations to Well Modeling,” CSUG/SPE 149489, presented at the Canadian Unconventional Resources Conference, Calgary, Alberta, Canada, 15-17 November.

Soeder, D.J.,1988, “Porosity and Permeability of Eastern Devonian Gas Shale,” SPE Formation Evaluation, pp. 116-124.

Tek, M.R., Coats, K.H., Katz, D.L., 1962, “The Effects of Turbulence on Flow of Natural Gas through Porous Reservoirs,” J. Pet. Technol. Trans. AIME 222, 799–806.

Wang, C., Didier Ding and Y.S. Wu, 2013, “Characterizing Hydraulic Fractures in Shale Gas Reservoirs Using Transient Pressure Tests”, SPE-163819 presented at SPE Hydraulic Fracturing Technology Conference, the Woodlands, TX, USA

Wang, F.P., R.M. Reed, J.A. Jackson, and K.G. Jackson, 2009. “Pore Networks and Fluid Flow in Gas Shales,” SPE 124253, presented at the 2009 SPE Annual Technical Conference and Exhibition held in New Orleans, Louisiana, USA, 4–7 October.

Warren, J. E., and P. J. Root, 1963, “The behavior of naturally fractured reservoirs”, Soc. Pet. Eng. J., Trans., AIME, 228, 245-255.

Wattenbarger, Robert A., El-Banbi, Ahmed H., Villegas, Mauricio E., and Maggard, J. Bryan, 1998, “Production Analysis of Linear Flow Into Fractured Tight Gas Wells”, SPE Rocky Mountain Regional/Low-Permeability Reservoirs Symposium, 5-8 April, Denver, Colorado.

Winterfeld, P. H. and Y.S. Wu, 2012a, “A Novel Fully Coupled Thermal-Hydrologic-Mechanical Model for CO2 Sequestration in Brine Aquifers,” submitted to and under review by International Journal of Rock Mechanics and Mining Sciences.

Winterfeld, P. H. and Y.S. Wu, 2012b, “A Novel Fully Coupled Geomechanical Model for CO2 Sequestration in Fractured and Porous Brine Aquifers,” presented at the XIX International Conference on Water Resources CMWR 2012, University of Illinois at Urbana-Champagne June 17-22.

Wu, Y.S., J. Li, Didier Ding, C. Wang, and Y. Di, 2013, "A Generalized Framework Model for Simulation of Gas Production in Unconventional Gas Reservoirs", SPE-163609 presented at the 2013 SPE Reservoir Simulation Symposium, the Woodlands, TX, USA

Wu, Y.S. and C. Wang, 2012, "Transient Pressure Testing Analysis of Gas Wells in Unconventional Reservoirs," SPE-SAS-312, presented at the 2012 SPE Annual Technical Symposium & Exhibition (ATS&E), Khobar, Saudi Arabia, 8-11 April.

Wu, Y.S., C, Wang, J. Li, and P. Fackahroenphol, 2012, "Transient Gas Flow in Unconventional Gas Reservoirs," SPE-154448, presented at the EAGE Annual Conference & Exhibition incorporating SPE Europec held in Copenhagen, Denmark, 4–7 June.

Wu, Y.S., 2002, "Numerical Simulation of Single-Phase and Multiphase Non-Darcy Flow in Porous and Fractured Reservoirs," Transport in Porous Media, Vol. 49, No. 2, 209-240.

Wu, Y.S. 2000, "A Virtual Node Method for Handling Wellbore Boundary Conditions in Modeling Multiphase Flow in Porous and Fractured Media", Water Resources Research, 36 (3), 807-814.

Wu, Y.S. 1998. MSFLOW: Multiphase Subsurface Flow Model of Oil, Gas and Water in Porous and Fractured Media with Water Shut-off Capability. Documentation and User's Guide, Walnut Creek, California.

Zimmerman, R.W., W.H. Somerton, and M.S. King, 1986, "Compressibility of Porous Rocks," J. Geophys. Res., Vol. 91,No. B12, pp.12,765–12,777.

APPENDIX A: NEW PSEUDO-PRESSURE FORMULATION DERIVATION

Considering the Klinkenberg effects and gas adsorption, the conversation of mass for isothermal gas flow through a porous media is expressed as:

$$\nabla \cdot \left[\rho \frac{k(P)}{\mu(P)} \nabla P \right] = \frac{\partial}{\partial t} \left[\phi \rho + m_g(V) \right] \tag{A.1}$$

The pressure-dependent permeability for gas was expressed by Klinkenberg as:

$$k_g = k_\infty \left(1 + \frac{b}{P_g} \right) \tag{A.2}$$

where k_∞ is constant, absolute gas-phase permeability under very large gas-phase pressure (where the Klinkenberg effect is minimized); and b is the Klinkenberg b-factor, accounting for gas-slippage effect

The mass of adsorbed gas in formation volume, V, is described (Wu et al. 2012):

$$m_g(V) = \rho_K \rho_g f(P) \tag{A.3}$$

where $m_g(V)$ is absorbed gas mass in unit volume, ρ_K is rock bulk density; ρ_g is gas density at standard condition; f(P) is the adsorption isotherm function. If the adsorbed gas terms can be represented by the Langmuir isotherm (Langmuir, 1916), the dependency of adsorbed gas volume on pressure at constant temperature is given below,

$$f(P) = V_L \frac{P}{P + P_L} \tag{A.4}$$

where V_L is the gas content or Langmuir's volume in scf/ton (or standard volume adsorbed per unit rock mass); P is reservoir gas pressure; and P_L is Langmuir's pressure, the pressure at which 50% of the gas is desorbed.

For real gas,

$$\rho = \frac{M}{RT}\left[\frac{P}{Z(P)}\right] \tag{A.5}$$

Substitute Equations (A.2)-(A.5) into Equation (A.1),

$$\nabla \cdot \left[\frac{P\left(1+\frac{b}{P}\right)}{\mu(P)Z(P)}\nabla P\right] = \frac{\phi}{k_\infty}\frac{\partial}{\partial t}\left[\frac{P}{z(P)} + \frac{RT\rho_K\rho_g V_L P}{\phi M\left(P+P_L\right)}\right] \tag{A.6}$$

From the definition of the isothermal compressibility of gas:

$$c_g(P) = \frac{Z(P)}{P}\frac{d}{dP}\left[\frac{P}{Z(P)}\right] \tag{A.7}$$

Define the "compressibility" from the adsorption:

$$c_a(P) = \frac{Z(P)}{P}\frac{d}{dP}\left[\frac{RT\rho_K\rho_g V_L P}{\phi M\left(P+P_L\right)}\right] = \frac{Z(P)}{P}\frac{RT\rho_K\rho_g V_L P_L}{\phi M\left(P+P_L\right)^2} \tag{A.8}$$

Let the total compressibility:

$$c_t(P) = c_a(P) + c_g(P) \tag{A.9}$$

Equation (A.6) will be:

$$\nabla^2 P^2 - \frac{d\left[\ln \frac{\mu(P)Z(P)}{1+b/P}\right]}{dP^2}\left(\nabla P^2\right)^2 = \frac{\phi\mu(P)c_t(p)}{k\left(1+b/P\right)}\frac{\partial P^2}{\partial t} \qquad \text{(A.10)}$$

Assume the viscosity and gas law deviation factors change slowly with pressure changes; the second part of Equation (A.10) becomes negligible. Equation (A.10) becomes:

$$\nabla^2 P^2 = \frac{\phi\mu(P)c_t(p)}{k\left(1+b/P\right)}\frac{\partial P^2}{\partial t} \qquad \text{(A.11)}$$

The new pseudo-pressure m(P) is defined as follows:

$$m(P) = 2\int_{P_0}^{P} \frac{P'(1+b/P)}{\mu(P)Z(P)}dP' \qquad \text{(A.12)}$$

Equation (A.1) can be rewritten in terms of variable m(P) using the definition of $C_t(P)$ given by Equations (A.7), to (A.9) as

$$\nabla^2 m(P) = \frac{\phi\mu(P)c_t(P)}{k(P)}\frac{\partial m(P)}{\partial t} \qquad \text{(A.13)}$$

This form of the flow equation (Equation (A.11)), is more appropriate the analysis of real gas flow behavior in unconventional reservoirs.

APPENDIX B: ANALYTICAL SOLUTION FOR GAS FLOW WITH KLINKENBERG

In this case, one dimensional linear flow is studied. The injection is set on the left side with constant rate and production part is on the right side with constant pressure. When the system reaches steady state, below are the equations to characterize the above flow models:

Permeability with Klinkenberg effects:

$$k = k_{\infty}(1 + \frac{b}{P}) \tag{B.1}$$

Mass conservation equation:

$$\rho v A = Q_m \tag{B.2}$$

Darcy's law:

$$v = -\frac{k}{\mu}\nabla P \tag{B.3}$$

Ideal gas equation:

$$\rho = \alpha P \tag{B.4}$$

Under one-dimensional, linear, horizontal, and steady-state flow condition, the boundary conditions are: a constant mass injection rate Q_m is imposed at the inlet (x=0) and the gas pressure is kept constant at the outlet (x=L). Combining equations (B.1) to (B.4), we get:

$$-A\alpha\frac{k_\infty}{\mu}(P+b)\frac{dP}{dx}=Q_m \tag{B.5}$$

Two boundary conditions are:

$$P(x=L)=P_L \tag{B.6}$$

$$-\rho A\frac{k}{\mu}\left(\frac{\partial P}{\partial x}\right)_{P=0}=Q_m \tag{B.7}$$

Solve the ODE Equation (B.5) with above two boundary conditions and the solution is:

$$P(x)=-b+\sqrt{b^2+P_L^2+2bP_L+\frac{2Q_m\mu(L-x)}{k_\infty A\alpha}} \tag{B.8}$$

APPENDIX C: ANALYTICAL SOLUTION FOR GAS NON-DARCY FLOW

Mass balance equation and ideal gas expression keep same with the ones mentioned in Appendix B, Equation (B2) and (B.4). Forchheimer flow but not Darcy's law is used to describe the relation between velocity and pressure gradient:

$$-\nabla P = \frac{\mu}{k} v + \beta \rho v |v| \tag{C.1}$$

Transform Equation (C.1),

$$\beta \rho v^2 + \frac{\mu}{k} v + \frac{\partial P}{\partial x} = 0 \tag{C.2}$$

$$v = \frac{-\frac{\mu}{k} + \sqrt{\left(\frac{\mu}{k}\right)^2 - 4\beta\rho\frac{\partial P}{\partial x}}}{2\beta} \tag{C.3}$$

Substitute the mass conservation equation and ideal gas equation into Equation (C.3) and get:

$$\frac{-\frac{\mu}{k} + \sqrt{\left(\frac{\mu}{k}\right)^2 - 4\beta\rho\frac{\partial P}{\partial x}}}{2\beta} = \frac{Q_m}{A} \tag{C.4}$$

Assume $c_1 = 2\beta\frac{Q_m}{A}$,

$$c_1 + \frac{\mu}{k} = \sqrt{\left(\frac{\mu}{k}\right)^2 - 4\beta\rho\frac{\partial P}{\partial x}} \tag{C.5}$$

$$\left(c_1^2 + 2c_1\frac{\mu}{k}\right)(L - x) = 2\alpha\beta\left(P_x^2 - P_L^2\right) \qquad \text{(C.6)}$$

The analytical solution is:

$$P_x = \sqrt{\frac{c_1^2 + 2c_1\frac{\mu}{k}}{2\alpha\beta}(L - x) + P_L^2} \qquad \text{(C.7)}$$

APPENDIX D: ANALYTICAL SOLUTION FOR GAS FLOW WITH ADSORPTION

If the system is isothermal, the ideal gas law applies, and gravity effect is negligible, then gas flow in porous media with adsorption is described by the following equations,

$$\nabla \cdot (\rho v) = -\frac{\partial (\phi \rho + m_g)}{\partial t} \tag{D.1}$$

where ρ is the gas density; v is the gas flow velocity; ϕ is the porous media porosity; m_g is the adsorbed gas mass in a unit formation volume at given pressure; and t is the time.

According to the ideal gas law,

$$PV = nRT \tag{D.2}$$

$$\rho = \frac{M}{RT} P = \beta P \tag{D.3}$$

where M is gas molecular weight; R is universe gas constant; and β is a coefficient, for simplicity, defined as $\beta = \frac{M}{RT}$; T is the system temperature.

From Darcy's Law and Langmuir isotherm,

$$v = -\frac{k}{\mu} \nabla P \tag{D.4}$$

$$m_g = \rho_R \rho_g V_E = \rho_R \rho_g V_L \frac{P}{P + P_L} = V \alpha \frac{P}{P + P_L} \tag{D.5}$$

where ρ_R is rock bulk density; ρ_g is gas density at standard condition; V_E is the adsorption isotherm function for gas content; V_L is the Langmuir's volume in scf/ton; and P_L P_L is Langmuir's pressure. α is a coefficient, for simplicity, defined as $\alpha = \rho_R \rho_g V_L$

Substituting Equations (D.4) and (D.5) into Equation (D.1), we will have

$$\nabla \cdot \left(\beta \frac{k}{\mu} P \nabla P \right) = \phi \beta \frac{\partial P}{\partial t} + \alpha \frac{\partial \left(\frac{P}{P + P_L} \right)}{\partial t} \tag{D.6}$$

In the radial coordinate,

$$\frac{1}{r} \frac{\partial}{\partial r} \left(r \frac{\partial P^2}{\partial r} \right) = \frac{2\phi\mu}{k} \frac{\partial P}{\partial t} + \frac{2\alpha\mu}{\beta k} \frac{\partial \left(\frac{P}{P + P_L} \right)}{\partial P} \frac{\partial P}{\partial t} \tag{D.7}$$

$$\frac{1}{r} \frac{\partial}{\partial r} \left(r \frac{\partial P^2}{\partial r} \right) = \left[\frac{2\phi\mu}{k} + \frac{2\alpha\mu}{\beta k} \frac{P_L}{\left(P + P_L \right)^2} \right] \frac{\partial P}{\partial t} \tag{D.8}$$

$$\frac{1}{r} \frac{\partial}{\partial r} \left(r \frac{\partial P^2}{\partial r} \right) = \left[\frac{\phi\mu}{Pk} + \frac{\alpha\mu}{P\beta k} \frac{P_L}{\left(P + P_L \right)^2} \right] \frac{\partial P^2}{\partial t} \tag{D.9}$$

The equation becomes:

$$\frac{1}{r} \frac{\partial}{\partial r} \left(r \frac{\partial P^2}{\partial r} \right) = \frac{1}{A} \frac{\partial P^2}{\partial t} \tag{D.10}$$

The coefficient $\frac{1}{A}$ is defined as:

$$\frac{1}{A}=\frac{\phi\mu}{\bar{P}k}+\frac{\alpha\mu}{\bar{P}\beta k}\frac{P_L}{\left(\bar{P}+P_L\right)^2} \tag{D.11}$$

A history-dependent, constant and average pressure within the pressure changed domain (Wu et al. 1998),

$$\bar{P}\approx\frac{\sum V_j P_j}{\sum V_j} \tag{D.12}$$

where V_j is a controlled volume at the geometric center of which the pressure was P_j at the immediate previous time when the solution was calculated. The summation, $\sum V_j$, is done over all V_j where pressure increases (or decreases) occurred at the previous time value. P_j is always evaluated analytically at point j, based on the previous estimated, constant diffusivity.

The well boundary proposed as a line source/sink well:

$$\lim_{x\to 0}\frac{\pi khr\beta}{\mu}\frac{\partial P^2}{\partial r}=Q_m \tag{D.13}$$

Then transient pressure solution for gas flow with adsorption/desorption is,

$$P^2(r,t)=P_i^2-\frac{\mu Q_m}{2\pi khr\beta}Ei(-\frac{r^2}{4At}) \tag{D.14}$$